Search for the Standard Model Higgs Boson at LEP200 with the DELPHI Detector

Vidar Lund

Department of Physics

University of Oslo

May 1, 1996

Thesis submitted in partial fulfillment of the requirements to obtain the degree of Cand. Scient. at the University of Oslo

Abstract

This thesis is dedicated solely to the coming search for the Standard Model Higgs Boson at LEP200. Moreover the study is limited to a particular channel of the Higgs signal, the $H^0\nu\bar{\nu}$ channel. As this channel is only 20% of the total Higgs signal, and the background is rather severe, it proves difficult to base a Higgs search on this channel alone, but added to other searches, in the lepton and quark channels of the Higgs signal, it will be most helpful. This search is based entirely on events simulated by the Monte Carlo program DELSIM. LEP200 configurations of $E_{cms} = 175$, 192 and 205 GeV are discussed, but after this study started, the 205 GeV option was omitted by the LEP Committee at CERN. Luckily the scheduled upgrade of LEP, to $E_{cms} = 192$ GeV in May 98, was approved recently. LEP will also run at $E_{cms} = 175$ GeV soon, but the integrated luminosity of this run will be far less than the 500 pb^{-1} used in this study.

Acknowledgements

I would like to thank my supervisors Alex Read and Lars Bugge, for being very helpful in all parts of this Higgs study. In addition, Ole Röhne and Trond Myklebust have been very helpful in implementing the analysis on full data simulations. Finally I would also like to thank my brother, Esben Lund, for valuable comments and suggestions.

Contents

Chapter 1

Introduction

Many aspects of particle physics have been thoroughly investigated in recent years, and great progress has been made. Many new particles have been discovered, and with them, new particle properties. Gell-Mann's quarks, the electroweak theory and enormous improvements of accelerators and detectors, promised the possibility of a complete description of nature, at least at small distance scales. But nature wanted it different. The problem of integrating different theories, especially general relativity and quantum mechanics turned out to be a head-on collision with reality! Many young physicists grew grey hair in those days, trying to figure out the physical implementation of string theory and supergravity. Lately the optimism concerning the synthesis of all theories into one have cooled, and more emphasis has been put on less extensive, but yet very important fields. The field considered by many as the most important is the problem of mass.

Though mass is of the utmost importance in all physical theories, its nature is mysterious. The mass is not merely some new quantum number with a simple associated operator like the spin of a particle. There seems to be no elementary mass quantum, like the elementary charge, which all other masses are multiples of. Many particle physicists believe, or want to believe, that the masses of different particles are not merely random numbers generated in the mind of God. If so they will always be free parameters in the laws of particle physics, only limited by actual observations of nature. Particle physicists try to find laws relating the masses of different particles in a hopefully understandable way. The most promising theory so far seems to be that of Peter Higgs, presented thirty years ago. Higgs introduced a field, later called the Higgs field, present everywhere in space, also in vacuum. The associated field boson is called the Higgs boson. The idea is that without this additional field the elementary particles would have no mass, but the particles interact with the Higgs field, with various strengths, thereby obtaining their characteristic masses. A particle heavily interacting with the Higgs boson will obtain a large mass, while the electron, almost invisible to the Higgs field, will be virtually massless. The Higgs bosons also interact among each other, in various loop diagrams, thereby obtaining mass themselves. Chapter 3 contains a further discussion on the Higgs theory.

Many particle physicists dislike the introduction of a new field, and draw parallels to the ether, but this does not stop all those intrigued by the possibility of finding an entirely new mechanism of mass generation. With the development of new accelerators, particularly LEP and LEP200, and the approval of the Large Hadron Collider (LHC), there has been a surge in Higgs hunting activities. The most thorough study yet, at LEP, rules out a Higgs boson of less than 65 GeV mass, at 95% confidence level [1]. The search will continue at LEP200, the future upgrade of LEP, which is the subject of this thesis. In the years after the first presentation of the Higgs theory, a swarm of different related theories have emerged, mainly concerning supersymmetric extensions of the theory, but they are only mentioned briefly in this thesis. The $H^0\nu\bar{\nu}$ channel of the Standard

Model Higgs production is studied at center of mass energies of 175, 192 and 205 GeV. LEP will be upgraded to $E_{cms} = 192$ GeV in May 1998, but a further upgrade to $E_{cms} = 205$ GeV was not approved by the LEP Committee at CERN.

Chapter 2

The LEP200 accelerator and the Delphi detector

2.1 The LEP200 accelerator

The Large Electron Positron (LEP) collider at CERN was originally designed to run at beam energies of ~46 GeV, the energies required for the production of Z^0 bosons. It's a synchrotron of 27 km circumference assembled in a circular tunnel situated underground between the Jura mountains and the airport of Geneva. Bunches of electrons and positrons are accelerated in opposite directions inside a single vacuumized beam pipe. After running at 46 GeV for several years, it has become increasingly interesting to run at higher energies. Two options have been of main interest;

- To run at ~80 GeV to produce W pairs.
- To run at maximum obtainable energy in the hunt for the Higgs boson.

The Higgs hunting has received most attention, in the scientific community at CERN. After a few years of planning and tests, the first preparations for the high-energy run of LEP have already started. In the autumn of 1995, LEP was prepared for a 70 GeV run, and during October and November, 5 pb^{-1} of integrated luminosity were delivered at this energy. In May 98 the proposed beam energy of 96 GeV will be reached. The upgrade of LEP is mainly a matter of inserting more RF cavities into the ring, but rapidly increasing synchrotron radiation of the accelerating electron beams prevents further upgrades beyond LEP200. The maximum obtainable beam energy of LEP is thought to be approximately 105 GeV, but practical problems and cost limitations lowers the actual upgrade proposal to 96 GeV.

2.2 The DELPHI detector

There are eight crossing points of the beams along the LEP accelerator ring, but detectors are located only at four points. The four detectors are OPAL, L3, ALEPH and DELPHI[2]. This thesis is concerning Higgs search at the DELPHI detector which has been operational since 1989. Since then, there have been some changes, the most important being the installation of STIC, described below, and the upgrade of the micro vertex detector. The DELPHI detector naturally consists of many sub-detectors of varying size and complexity. Various parts of the DELPHI detector, sketched in Fig. 2.1, are described briefly below:

Micro Vertex Detector, VD This is a silicon-strip detector, with three layers. At first it had $R\phi$-coverage down to 43° in the forward direction, but in the expanded 1996 version it has coverage down to 25° in the forward direction, and some of the silicon modules are double layered, giving information about the z coordinate too. It's very small, only 46 cm long, and with a diameter of just 22 cm. Resolution of the detector in $R\phi$ is 5 μm, with a

readout pitch of 50 μm, while resolution and readout pitch in the z direction varies depending on the incident angle θ. In the forward direction, at θ ranging from 25° to 38°, the readout pitch is 150 μm with a resolution of 30 μm at 38° and 50 μm at 25°. At angles of 38° to 58°, the readout pitch is 100 μm and the resolution is improved to approximately 20 μm. At 58° to 90° the pitch is further improved to 50 μm with an associated resolution of 10 μm. The tiny micro vertex detector is probably the most important in B physics and Higgs searches, as it provides excellent track and vertex reconstruction.

Inner Detector, ID The inner detector is a small drift chamber situated outside of the micro vertex detector. Resolution in $R\phi$ is 90 μm, and 5 cylindrical layers of circular cathode strips provide additional resolution of 1 mm in the z direction. The inner detector provides trigger information and track reconstruction. Efficiency for the drift chamber is above 90% for jet events, and the outer layers give >95% trigger efficiency for single tracks.

Time Projection Chamber, TPC This is a very useful detector in any analysis at DELPHI. It's basically a barrel shaped box, filled with gas and field shaping wires. It's positioned outside the inner detector. Tracks of charged particles are reconstructed in an accurate way, useful for determining momenta of particles associated with tracks curved by the magnetic field of the superconducting solenoid. Resolution is 0.23 mm in $R\phi$, and 0.9 mm in z.

Outer Detector, OD The outer detector, composed of 24 modules, mounted on the barrel RICH, and each containing 145 drift tubes in 5 layers, provides fast trigger information and improved momentum resolution, particularly for fast particles. Tracks of fast particles are only slightly curved in the time projection chamber, making momentum calculations based on track curvature very uncertain. As such the outer detector becomes an extension of the TPC, added to overcome part of the problems caused by the reduction of the TPC, due to introduction of the barrel RICH. It becomes possible to extrapolate tracks from the TPC, into the outer detector, to determine curvatures in a much more precise way. Resolution is 0.11 mm in $R\phi$, and 4.4 cm in z.

Ring Imaging Cherenkov counter, RICH This is one of the most complex designs at DELPHI. It's a combined gas and liquid Cherenkov detector, situated outside of the TPC, and with separate modules in the forward direction. For several years this detector was almost not used, because of technical problems, but now it turns out to be one of the most prominent detectors and it has been of great use lately, particularly in B physics. The RICH is very useful in conjunction with the TPC and OD, described

above. Tracks of charged particles are reconstructed using the TPC and OD, allowing accurate measurements of momenta as previously described. On the other hand, the RICH measures speeds, and not momenta of the same particles. Knowing both speeds and momenta of the charged particles, calculation of their masses becomes trivial. This makes the RICH perfect for hadron identification, as separation of π mesons, K mesons and protons, becomes possible using mass calculations.

High density Projection Chamber, HPC This is an electromagnetic calorimeter, placed outside of the RICH. The calorimeter is especially designed to measure the energies of electrons and photons. It's one of the first large-scale applications of a time-projection chamber in calorimetry. This means that the HPC is a gas detector based on the same principles as the TPC. Instead of using the ionized gas, left by a passing particle, for track reconstruction, the amount and distribution of the ionized gas is used for estimation of the energy of the passing particle. Electrons and photons are often totally stopped by the lead walls of the HPC, depositing all of their energy within the detector. The dynamical range of the detector allows electromagnetic showers of up to 50 GeV with, simultaneously, full sensitivity to minimum ionizing particles. The HPC only covers the barrel region down to incident angles, θ, of 43°, and the shower resolution is $23\%/\sqrt{E} + 1.1\%$. Readout granularity is $\sim$1° in ϕ, and 4 mm in z.

Hadron calorimeter This detector constitutes the bulk of the DELPHI detector. It's a very heavy gas calorimeter, situated outside of the superconducting solenoid and in the two end-caps. The barrel is constructed of 24 sectors, with 20 layers of limited streamer mode detectors inserted into 2 cm slots between the 5 cm thick iron plates. The calorimeter is not very accurate and it has a large granularity, making it hard to separate nearby tracks. As the name suggests, it's used to measure energies of hadrons like protons, neutrons and K mesons. The hadron calorimeter is also useful for muon detection, as most particles, except muons, are stopped by the iron plates of the calorimeter. This makes the calorimeter act as a filter, that removes all particles but the muons and some π mesons. Dedicated muon chambers are placed around the entire detector, outside of the hadron calorimeter, to detect the escaping muons. Shower resolution of the hadron calorimeter is $120\%/\sqrt{E}$. Readout granularity is 3.75° in ϕ, and 3.0° in θ.

Forward Chambers A, FCA The forward chamber A provides tracking and triggering for θ=33° down to θ=11°. The double layered streamer chamber is mounted on the end of the TPC. Resolution of the detector is $\sim$0.3 mm, and the trigger efficiency for single tracks is $\sim$95%.

Forward Chambers B, FCB This gas detector is placed between the forward RICH and the FEMC, described later. It provides precise tracking and the resolution in the plane of the detector is 120 μm. It covers incident angles, θ, of 35° down to 11°.

Forward Electro-Magnetic Calorimeter, FEMC This electromagnetic calorimeter was designed to give good energy resolution and granularity in the forward direction. It covers angles, θ, ranging from 36.5° down to 10°. The FEMC consists of two disks, of 5 m diameter, with a total of 9064 lead glass blocks shaped as truncated pyramids, arranged to point towards the interaction point. Readout granularity is 1° in ϕ and 1° in θ, and the energy resolution is 4% for Bhabha scattered electrons at 45.6 GeV.

STIC This is the low angle calorimeter, covering incident angles, θ, of 10.3° down to just 1.7°, that replaced the less accurate SAT detector. The calorimeter consists of tiled layers of lead with scintillators in between. The layers of scintillator plates are cut into 10 rings, each with 16 sectors, and contrary to the old detectors of DELPHI, the STIC has been optimized for LEP200 physics. This means that it will be able to handle Bhabha scattered electrons of ~96 GeV energy, much better than the previous SAT detector, which was optimized for electrons of only 46 GeV energy. The important luminosity determinations are based on measurements of Bhabha scattered electrons. Energy resolution at 45 GeV is as good as 3%.

Forward and Barrel Muon chambers, FMU and BMU The barrel muon detector is composed of 2 layers. The first layer of 48 muon detectors is inserted into the hadron calorimeter, with 90 cm of iron separating the interaction point and the muon chambers. Each muon detector is shaped as a long plank, and contains 3 staggered drift chamber planes. The second layer of muon chambers is mounted on the outside of the hadron calorimeter, behind a further 20 cm of iron. This layer consists of overlapping muon chambers, each containing two staggered planes of drift chambers. Resolution is ~1 mm in $R\phi$, and ~10 mm in z, and the individual chamber efficiency is ~95%. Overall efficiency for a muon track, with typically 4 hits per track, is therefore high. The forward muon detectors also have two layers of chambers, one inside the forward hadron calorimeter, and one mounted on the outside of it. Each layer or plane, covering ~80 m^2, is composed of 4 quadrants consisting of 2 orthogonal layers of 22 drift chambers. Defining a xy-plane in the plane of the muon detector, resolution is ~1 mm in both directions. The efficiency per detector layer, averaged over all layers, is ~89%, but again a single muon will pass several muon chambers (4 detector layers), giving a much better overall efficiency. As previously discussed the hadron calorimeter removes all particles, but the muons and a few π mesons. These escaping muons are detected in the muon chambers

surrounding the entire detector, thereby allowing separation of muons from other particles.

Time of Flight counters, TOF The time of flight counters serve as fast trigger for beam events and cosmic events and may be used to veto cosmic muons during beam crossings. The TOF system in the barrel region consists of a single layer of 172 counters mounted on the inside of the return yoke just outside the solenoid. Each counter is 355 cm long, 19 cm wide and 2 cm thick. They are made of plastic scintillators wrapped in aluminium foils. In the forward region, the TOF system, also called the forward hodoscope, has a similar design as in the barrel region. It consists of long plastic scintillators, mounted to form a single scintillator plane of $\sim$70 m^2. The forward hodoscope is mounted between the end-cap yoke and the second muon chamber layer.

40° taggers During the 1993/94 LEP shutdown, the first scintillator-lead counters were installed at three different positions in the intersection between the barrel and the forward RICH, inside the DELPHI detector, to give maximum angular coverage. Their purpose is to tag the electromagnetic energy which escapes detection in the cracks between the barrel and the end caps, thus improving the detector hermiticity. As later shown, this is particularly important for LEP200 data taking when missing energy will play a major role. Each counter consists of a 2 cm thick lead plate and a 1 cm thick scintillator. Detailed studies of the 40° taggers [3], reveal that they are unfortunately not capable of providing reliable energy estimates. They are never the less useful in this Higgs study, as Chapter 6 will show.

Superconducting coil The superconducting solenoid is placed between the HPC and the hadron calorimeter. It has a length of 7.4 m, and an inner diameter of 5.2 m. A field of 1.2 T is produced by a 5000 A current running through the aluminium wire of the solenoid. It's the powerful magnetic field that causes bending of tracks of charged particles, allowing determination of particle momenta and charges. The coil is cooled by flowing liquid helium.

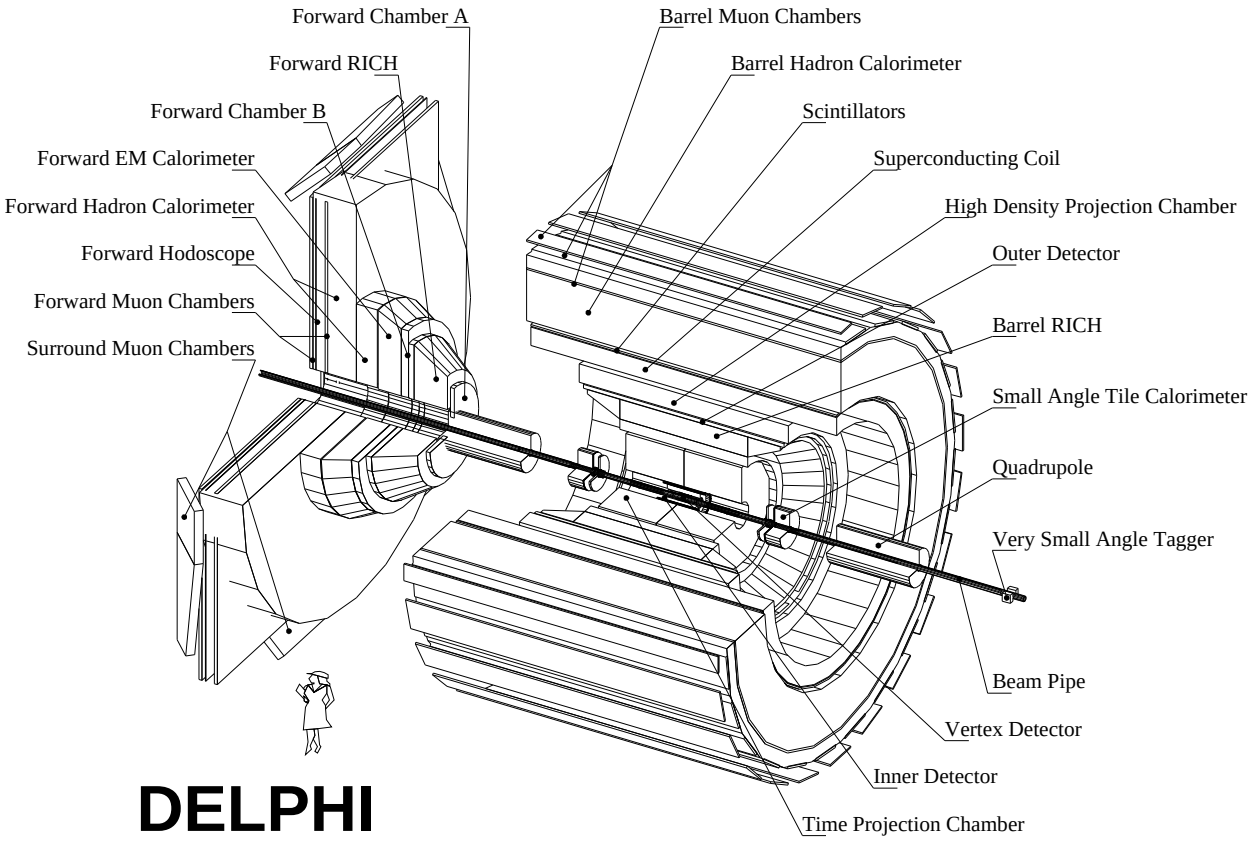

Figure 2.1: The DELPHI detector.

Chapter 3

Standard Model Higgs theory and possible Higgs production at LEP200

3.1 Standard Model Higgs theory

Formulas and most theoretical considerations of this chapter have been taken from the book called *The Higgs Hunter's Guide* [4]. The Higgs mechanism was first suggested by Peter Higgs[5] in 1964 as a way to explain how the gauge bosons of the electroweak part of the Standard Model obtain mass. Recall that Quantum Chromo Dynamics (QCD), now included in the Standard Model, was not developed in 1964. The Higgs mechanism has its direct physical manifestation in a single boson called the Higgs boson. The Standard Model is a gauge theory, and the SU(2)×U(1) gauge invariance of the electroweak part of the theory requires masses of the gauge bosons to be zero, since the presence of a mass term for the gauge bosons violates gauge invariance ($M^2 A_\mu A^\mu$ is not invariant if $A_\mu \to A_\mu - \partial_\mu \chi$ where χ is a function of position in spacetime, so M^2 must be zero). The Higgs mechanism circumvents this constraint by beginning with a gauge invariant theory having massless gauge bosons, and ending with a spectrum having massive gauge bosons, after algebraic transformations on the Lagrangian. The physics leading to a gauge boson mass and a physical Higgs boson is contained in the Abelian case, which follows in a brief description.

Assume there exists a complex scalar boson ϕ and a massless gauge boson A^μ. Assume the Lagrangian of the theory has the form

$$\mathcal{L} = (D_\mu \phi)^* (D^\mu \phi) + \mu^2 \phi^* \phi - \lambda (\phi^* \phi)^2 - \frac{1}{4} F^{\mu\nu} F_{\mu\nu}$$

The parameters are constrained by $\lambda > 0$ (so that the potential is bounded from below), and $\mu^2 > 0$. $F^{\mu\nu}$ is the antisymmetric tensor of the gauge boson field, $F^{\mu\nu} = \partial^\mu A^\nu - \partial^\nu A^\mu$. Invariance of the theory under a local gauge transformation,

$$\phi \to \phi' = e^{ig\chi(x)} \phi$$

$$A^\mu \to A'^\mu = A^\mu - \partial^\mu \chi(x)$$

is guaranteed if in the Lagrangian we use the covariant derivative $D^\mu = \partial^\mu + igA^\mu$, in place of the ordinary partial derivative ∂^μ. The potential for the scalar field has its minimum value at $\phi = v/\sqrt{2} = \sqrt{\mu^2/2\lambda}$. It is appropriate to expand ϕ near its minimum to find the spectrum of the theory, so write

$$\phi = \frac{v + h(x)}{\sqrt{2}}$$

where $h(x)$ is a real field. Substituting this into $\mathcal{L}$, we have explicitly

$$\mathcal{L} = \frac{1}{2}[(\partial_\mu - igA_\mu)(v + h)(\partial^\mu + igA^\mu)(v + h)]$$

$$+ \frac{1}{2}\mu^2 (v + h)^2 - \frac{1}{4}\lambda (v + h)^4 - \frac{1}{4} F^{\mu\nu} F_{\mu\nu}$$

This contains several important terms. There is a term $(g^2v^2/2)A_\mu A^\mu$ that should be interpreted as a mass term for the gauge boson. There is a term $-\lambda v^2 h^2$ that is a mass term for the scalar boson. There are interaction terms h^3, h^4, hAA, and h^2AA, with related strengths. The theory with a complex scalar boson and a massless gauge boson has been reinterpreted as a theory with a real scalar boson and a massive gauge boson, because the scalar potential had its minimum at a value of ϕ that was non-zero. This way of giving mass to the gauge boson is called the Higgs mechanism.

Four things should be emphasized for our purposes. First there is a real boson, h, that should occur as a physical boson, the Higgs boson. Second, its mass depends on λ and on v. The gauge boson mass determines v, but the λ is a parameter characteristic of the scalar potential and no one has ever found a way to calculate or determine λ without finding experimental information about the Higgs spectrum itself. Therefore the mass of the Higgs boson is unknown. Third, the interaction terms (plus those that occur when fermions are given mass) determine the production mechanisms and decays of the Higgs boson. The self-interaction terms depend on λ but the terms describing the interaction of h with A do not depend on λ, so their strength is known. Fourth, the counting of the number of independent states is consistent. This example began with one complex scalar field ϕ, having two real fields since it's complex. The massless gauge boson had two polarization states, just as a photon would. After the reinterpretation, there is one real Higgs boson, plus the three polarization states ($J_Z = 1, 0, -1$) of a massive spin-one boson. In both cases the total number of degrees of freedom is four.

Continuing the counting, when we consider the Standard Model we add an SU(2) internal quantum number to the Higgs fields, so there is an SU(2) doublet of complex scalars, with four real fields. There are three massless gauge bosons, $W^\pm$ and Z, with two polarization states each, so the total number of independent fields is ten. Symmetry breaking is initiated by giving a vacuum expectation value $<\phi^0> = v/\sqrt{2}$ to the neutral Higgs field. The result is three massive gauge bosons, with nine degrees of freedom, so there will be one physical Higgs boson that should appear as a real particle.

In a supersymmetric theory the added symmetry implies that two SU(2) doublets of complex Higgs fields are required to give mass to fermions, so there will be eight real scalar fields, plus six massless gauge boson degrees of freedom, fourteen in total. After the Higgs mechanism operates the same nine states are required for the gauge bosons, so five real fields remain, and there should be five spin-zero Higgs fields in the spectrum. This is one of the many experimentally checkable predictions of the Minimal Supersymmetric Model. In this case, three of the scalar bosons are neutral (the h^0, A^0 and H^0) while the other two are a charged pair (H^+ and H^-).

Any theory with additional physics beyond the Standard Model will have a spectrum of spin-zero Higgs fields (one or two more states, SU(2) singlets or dou-

blets or triplets, etc.) that leads to a specific number of spin-zero bosons. In addition, definite relations (often depending on parameters with completely unknown values) hold between masses and coupling strengths of the various bosons. Ultimately it will be necessary to determine experimentally the full spectrum of scalar bosons, from zero-mass through the TeV region, in order to be confident that any particular theory is correct. Only by finding some spin-zero bosons, or by knowing conclusively that they are not present with the necessary couplings over various mass regions, will it be possible to achieve any consensus on what theory is correct. To arrive at a fully valid theory of the Higgs sector will require detailed and complete experimental information.

The problem with all Higgs theories is that they, as previously stated, contain one or several parameters of unknown value. These parameters can behave in very strange and unphysical ways, particularly in the Supersymmetric Models. Fortunately they all seem to have at least one light Higgs boson, which is supposed to be in the one TeV range. This means that the Large Hadron Collider, which will be able to produce very massive Higgses, will as far as possible settle the question, whether there is a Higgs sector or not. Detectors at LEP200 will be able to discover a neutral Higgs boson of up to 96 GeV mass, far less than the mass obtainable at LHC, but in an important energy region that is very hard to access at LHC, due to background problems.

In the Standard Model a single Higgs doublet can give mass to both the gauge bosons and the fermions. In supersymmetric theories, although there are two doublets, this aspect is basically unchanged. The two vacuum expectation values contribute in the combination $v_1^2 + v_2^2$ to the gauge boson masses, while down-type fermions have mass proportional to v_1 and up-type fermions have mass proportional to v_2. However, in non-supersymmetric models it is not necessary that the same Higgs field give mass to both fermions and gauge bosons, nor is it required that the Higgs fields that give mass to the up and down type quarks be different.

It is worthwhile looking at the role of Higgs bosons from a different point of view, following the arguments of Ref.[6]. If the process $f\bar{f} \rightarrow \mathrm{W^+W^-}$ is considered, when the produced W's are longitudinally polarized (those W's that arose above by the Higgs mechanism) there are contributions from s-channel gauge bosons and t- or u-channel fermions. If the couplings are in precisely the ratios required for a gauge theory, a term in the cross section that is quadratic in s vanishes, because of cancellations among the contributions. However, there is still a term in the cross section that grows as $m_f^2 s$. This is the piece cancelled by the contribution of an s-channel Higgs boson that couples proportional to m_f (by considering other channels, such as $\mathrm{WW} \rightarrow \mathrm{WW}$ the couplings can be uniquely determined). This argument makes clear the fact that a physical Higgs boson, or scalar interaction, must be included along with the gauge bosons to have a sensible theory. Without such a contribution, some amplitudes exceed their unitarity limits at large s. In addition, when tree-level processes which

violate unitarity appear as sub diagrams within higher loop diagrams of the theory, infinities result which cannot be removed by renormalization. The theory would, therefore, not be renormalizable. However, it could happen that the scalar interaction is not due to a single fundamental boson, but is generated by non-perturbative behavior of the theory. Whatever happens, some new spin-zero interaction must occur, and it can be discovered experimentally.

It should be emphasized that there are no definite theoretical upper or lower limits on Higgs boson masses relevant to experiments. A possible lower limit deriving from the requirement that the symmetry-breaking vacuum be the absolute minimum is dependent upon knowledge of fermion masses. For example, in the minimal Standard Model, when radiative corrections from gauge boson and fermion loops are included in the Higgs potential, there are two possible minima: the symmetric minimum at $\phi = 0$ and the symmetry-breaking minimum at $\phi = v/\sqrt{2}$. Insisting that the minimum at $\phi = v/\sqrt{2}$ be the lower one gives a condition

$$m_{\phi^0}^2 > \frac{3(2m_W^4 + m_Z^4) - 4\sum_l m_l^4 - 12\sum_q m_q^4}{16\pi^2 v^2}$$

where $v = (\sqrt{2}G_F)^{-1/2} \simeq 246$ GeV. Each particle enters in proportion to its number of charge, spin and color states. We sum over three generations of quarks (q) and leptons (l). If all fermions have small masses compared to m_W and m_Z, the above equation yields the bound $m_{\phi^0} > 7$ GeV. However, if a heavy fermion (e.g., the top quark) with $m_f \sim m_W$ exist, as the recent Fermilab results show, there is no lower limit on m_{ϕ^0}, even in this minimal model. Beyond minimal models, limits are more model dependant and generally apply only to a combination of scalar masses. For example, in the two-Higgs-doublet model, in the absence of information about scalar masses and mixing angles, there is only a lower limit for the heavier of the two neutral (CP-even) scalars. Any lower Higgs mass limit depends on assumptions about the fermion and boson spectra. Some lower limit will occur in any particular theory, but such lower limits should not be used to bias the manner in which experimental searches for scalar bosons are carried out.

The existence of a model independent upper limit on m_{ϕ^0} is less certain. In fact, it is entirely possible that no scalar particle exists which is sufficiently light to prevent some amplitudes of WW $\rightarrow$ WW from approaching their unitary limit, at which point the true theory must begin to differ from the perturbative predictions of the Standard Model. For large m_{ϕ^0}, the value of $\sqrt{s_{WW}}$ where significant non-perturbative behavior sets in differs from model to model, but is normally around 1.2 TeV. Sometimes this is described as an upper limit on m_{ϕ^0}, but it is perhaps most desirable to simply view this as being the scale where perturbative analysis ceases to be useful. At the present state of the art, it seems premature to limit the Higgs mass range over which experimental searches are conducted.

Figure 3.1 shows the possible production mode of Standard Model Higgs bosons at LEP200. A Higgs boson is radiated off a very massive Z^*, that re-

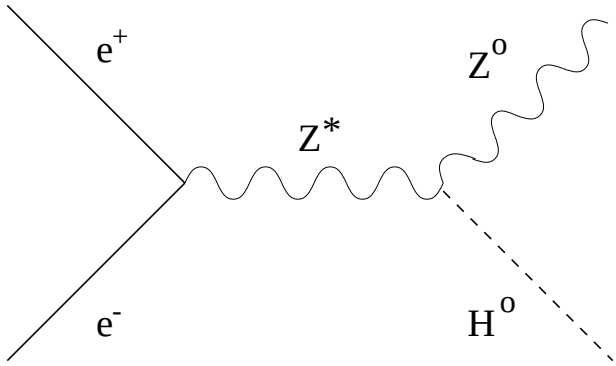

Figure 3.1: Higgs production through the Björken process.

turns to an on-shell Z^0 boson. This process was first described by J. Björken [7] in 1976. Table. 3.1 contains the cross section of the H^0Z^0 signal at 175, 192 and 205 GeV, for different Higgs masses, m_{H^0}. The calculations, done by Kniehl et al.[8], included several corrections to the tree level results. These were initial state bremsstrahlung to second order with exponentiation, finite width effects, and the full one-loop electroweak corrections to the underlying $e^+e^- \rightarrow H^0Z^0$ process. Further corrections are thought to be very small, only of the order of 1% or less. These cross sections will be used later in Chapter 7, but now attention is put on branching ratios of the Higgs boson. Since the couplings of ϕ^0 to fermions are proportional to the fermion mass, the decay branching ratio to any fermion f is proportional to m_f^2. The partial width to any fermion channel, at tree level, is

$$?\,(\phi^0 \rightarrow \bar{f}f) = \frac{N_c g^2 m_f^2}{32\pi m_W^2}\beta^3 m_{\phi^0}$$

where N_c is 1 for leptons and 3 for quarks, and $\beta^2 = -4m_f^2/m_{\phi^0}^2$. Thorough calculations, done by Kniehl et al.[8] and here presented in Table 3.2, have taken several corrections into account. These are two-loop QCD corrections to the hadronic widths, one-loop electroweak corrections to the fermionic widths, and the contributions from the $\gamma\gamma$, $\gamma^\star Z$, $Z^\star Z^\star$, and $W^\star W^\star$ channels.

The results differ considerably from the tree level calculations in the large $\tau^+\tau^-$ branching ratio and the relatively small $c\bar{c}$ ratio. These particular ratios are heavily affected by higher order loop corrections. At tree level, the $c\bar{c}$ branching ratio for a Higgs boson of $m_{H^0} = 80$ GeV is 8.5% while the $\tau^+\tau^-$ ratio is only 4.2%. The important $b\bar{b}$ branching ratio is however only changed from 87.3% to 87.1%, at $m_{H^0} = 80$ GeV, by higher order loop corrections.

After this rather thorough description of the Higgs boson, its branching ratios and the cross section of the H^0Z^0 signal, it's time to have a closer look at the background processes at LEP200.

E_{cms} (GeV)	m_{H^0} (GeV)	*cross section* (pb)
175	70	0.752
	80	0.283
	90	0.032
192	70	0.784
	80	0.594
	90	0.374
	100	0.083
205	70	0.704
	80	0.582
	90	0.450
	100	0.301

Table 3.1: Cross section of the H^0Z^0 signal at 175, 192 and 205 GeV. The cross sections are presented for different values of m_{H^0}.

m_{H^0}	$b\bar{b}$	$\tau^+\tau^-$	$c\bar{c}$	gg	$W^\star W^\star$	$Z^\star Z^\star$	$\gamma\gamma$
70	87.6	9.2	2.8	0.4	-	-	-
80	87.1	9.5	2.8	0.4	0.1	-	0.1
90	86.7	9.6	2.8	0.6	0.2	-	0.1
100	85.3	9.7	2.7	0.7	1.3	0.1	0.2
110	80.8	9.4	2.6	0.8	5.7	0.5	0.2

Table 3.2: Branching ratios of the Higgs boson at various masses relevant to the Higgs search at LEP200. The Higgs mass, m_{H^0}, is in units of GeV and the branching ratios are in %.

Chapter 4

Background processes at LEP200

4.1 Main backgrounds at LEP200

The Higgs signal at LEP200 is very small, only at the order of 0.5 pb or less, as shown in Chapter 3. This makes the signal very vulnerable to any background processes. Even though there are some big background processes causing difficulties, they are fortunately not of the character that completely blurs the signal. The most abundant background process, illustrated with a Feynman diagram in Fig. 4.1, is the production of fermion pairs, through annihilation of the colliding electrons. Most of this production, around 75%, comes from radiative return to the Z^0 boson, as shown in Fig. 4.2. This means that one, or both, of the colliding electrons radiate a very energetic photon in the initial state of the interaction. The photon radiation is such that the center of mass energy of the colliding electrons is lowered to around 91 GeV, the energy needed for production of a single on-shell Z^0. In Chapter 6, it's shown that this process is an important background to the neutrino channel of the H^0Z^0 signal, the channel treated in this thesis. The remaining 25% of the fermion pair production comes from annihilation of the electrons, without any powerful initial state radiation. This process, turns out to be a background to the four jet channel of the H^0Z^0 signal. The entire fermion pair production is referred to as the $\gamma^\star/Z^0$ process. The type of fermions that come from fermion pair production is governed by the decay modes of the Z^0 boson. This means that 70% of the fermions are quark pairs, 20% are neutrino pairs, and the last 10% are charged leptons.

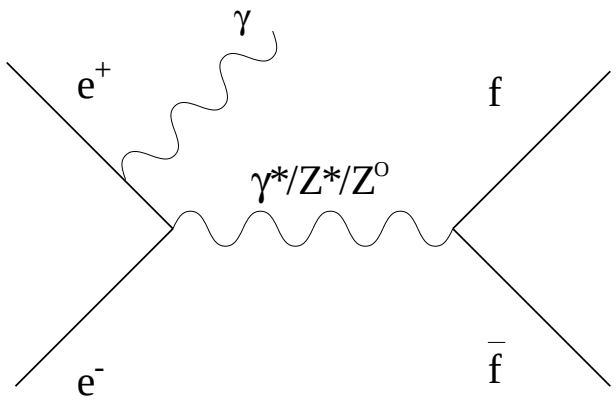

Figure 4.1: The $e^+e^- \to \gamma^\star/Z^0 \to f\bar{f}$ annihilation diagram.

The second most common background at LEP200 is the production of W pairs. The two production modes are shown in Fig. 4.3 and Fig. 4.4. This background is dangerous to all channels of the H^0Z^0 signal, but it is fortunately almost free of B jets, making it reducible by the B tagging procedure described in chapter 5. The production of W pairs itself, is considered to be one of the most interesting

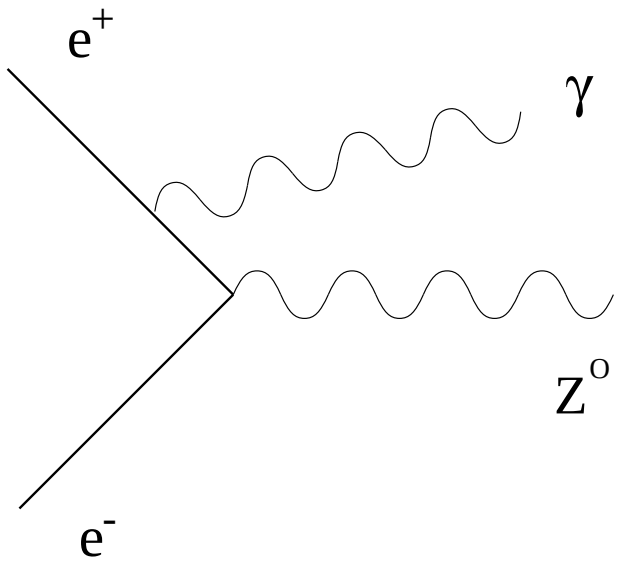

Figure 4.2: Radiative return to Z^0.

fields of study at LEP200, and some particle physicists hope that LEP200 will run at the peak of W pair production, at least for a while. This is a reasonable thing to do, even though it reduces the total integrated luminosity of the Higgs search a bit.

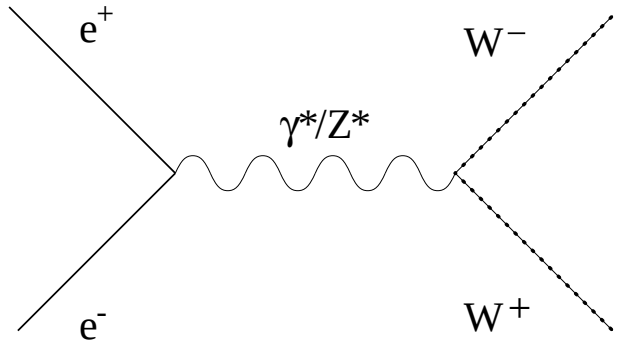

Figure 4.3: The $e^+e^- \rightarrow W^+W^-$ annihilation diagram.

Both the fermion pair, and W pair backgrounds are reducible, but one background is not, the Z^0Z^0 production by the conversion diagram shown in Fig. 4.5. Part of this background has all the characteristics of the H^0Z^0 signal, but its cross section is fortunately only a little bit bigger than that of the H^0Z^0 signal, making it possible to cope with. These are the most important backgrounds and some of

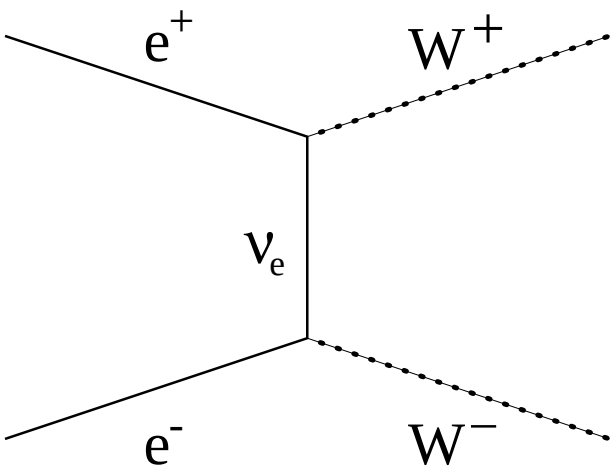

Figure 4.4: The $e^+e^- \rightarrow W^+W^-$ conversion diagram.

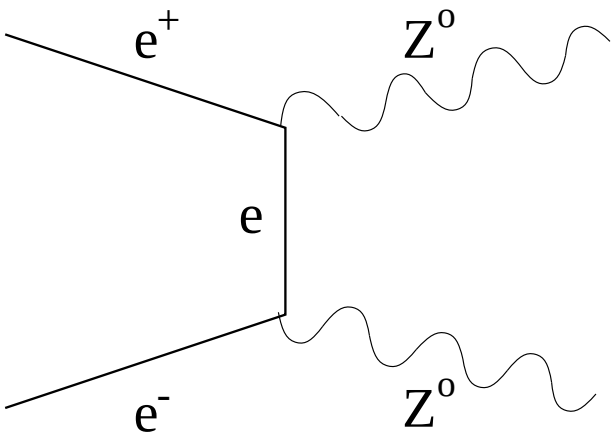

Figure 4.5: The $e^+e^- \rightarrow Z^0Z^0$ conversion diagram.

their characteristics. Characteristics of the Higgs signal will be discussed further in Chapter 5.

Other backgrounds, some of which are quite similar to the ones described above, are

- $e^+e^- \rightarrow (e^+e^-)f\bar{f}$
- $e^+e^- \rightarrow We\nu_e$
- $e^+e^- \rightarrow Z^0e^+e^-$
- $e^+e^- \rightarrow Z^0\nu\bar{\nu}$

The $(e^+e^-)f\bar{f}$ background has a rather big cross section, but it is very different from the H^0Z^0 signal, and thus of minor importance. The three other backgrounds are small and turns out to be handled nicely by the cuts imposed on the more severe backgrounds. This is discussed in chapter 7, where results of the full simulations are presented. The cross sections of the most important backgrounds, at the three chosen energies, are shown in Table 4.1. These cross sections were generated, with initial state radiation, using the Monte Carlo program PYTHIA[9].

E_{cms} (GeV)	σ_{γ^*/Z^0} (pb)	$\sigma_{W^+W^-}$ (pb)	$\sigma_{Z^0Z^0}$ (pb)
175	171	15.1	0.46
192	136	18.1	1.22
205	115	18.3	1.47

Table 4.1: Background cross sections.

Chapter 5

Monte Carlo Simulation of Higgs events

5.1 Why do simulations?

The most important work of the Higgs search at DELPHI is actually done before the high energy runs at LEP200 start. It's impossible to see tracks of Higgs bosons, because of their very short lifetimes. Only decay products of the Higgs bosons can be seen. These decay products will hopefully have special characteristics, like particular energies, or special angular distributions. These characteristics will then be used to confirm the presence, or absence, of Higgs events. To find such characteristics, extensive simulations of Higgs events, using a Monte Carlo program, have to be performed first. The program chosen was PYTHIA (containing JETSET[10]). To produce final simulation results, it's necessary to run a full DELPHI detector simulation called DELSIM[11], but this is very complex and time consuming, so most of the simulation work was done at generator level, only using PYTHIA. The full simulations are subject of the next chapter.

5.2 What do Higgs events look like?

The PYTHIA program produces a very extensive and complete list of all particles resulting from a single event. This list is easy to read, but it often contains hundreds of particles, and it's virtually impossible to perceive a vivid picture of a complicated event. A few graphical images of events were therefore created. One particularly nice event is presented in Fig. 5.2. It was generated at an energy of 192 GeV in the centre of mass system and with a Higgs mass of 80 GeV.

Fig. 5.1 shows a Higgs boson and a Z^0 boson decaying into four B mesons. The figure is in the xy plane of a Cartesian coordinate system, where the primary vertex defines the origo, and the beam pipe defines the z axis. It's only the remnants of the B mesons that are presented in the figure. The scale of the figure is in millimeters. The B mesons typically travel a few millimeters before they decay into D mesons and other particles. It's only long living particles that are presented by a line. The lines represent the momentum of particles, where their length is given in GeV/c. Shortlived particles are only seen as they decay, marked by a small circle, into lighter particles, mainly gammas and π mesons. First the Higgs boson and the Z^0 boson decay into four B mesons. All of these then decay into D mesons plus gammas and π mesons. The gammas and π mesons are visible, but the D mesons are not. They travel a few millimeters, except the one in the upper left corner of the figure which decays at once, and then they decay into K mesons plus gammas and π mesons. The decays of the K mesons usually happen outside the range of the figure.

Fig. 5.2 is the same as Fig. 5.1, except that all stable particles have been included. It's obvious that many particles come directly from the primary vertex, even though most come from the B jets. The particles from the primary vertex are coming from various resonances that quickly decay. These resonances are

produced during the fragmentation process of the initial quarks that the H^0 and Z^0 bosons decayed into. The particles from the primary vertex tend to head in one particular direction, which often results in a fifth jet, similar to the others. The jets of this event are very well defined, but often the B jets mingle into each other, and sometimes jets from the primary vertex may be dominant. Such cases are common, but fortunately, different routines, like the clustering routine LUCLUS[12], helps bring order to the mess.

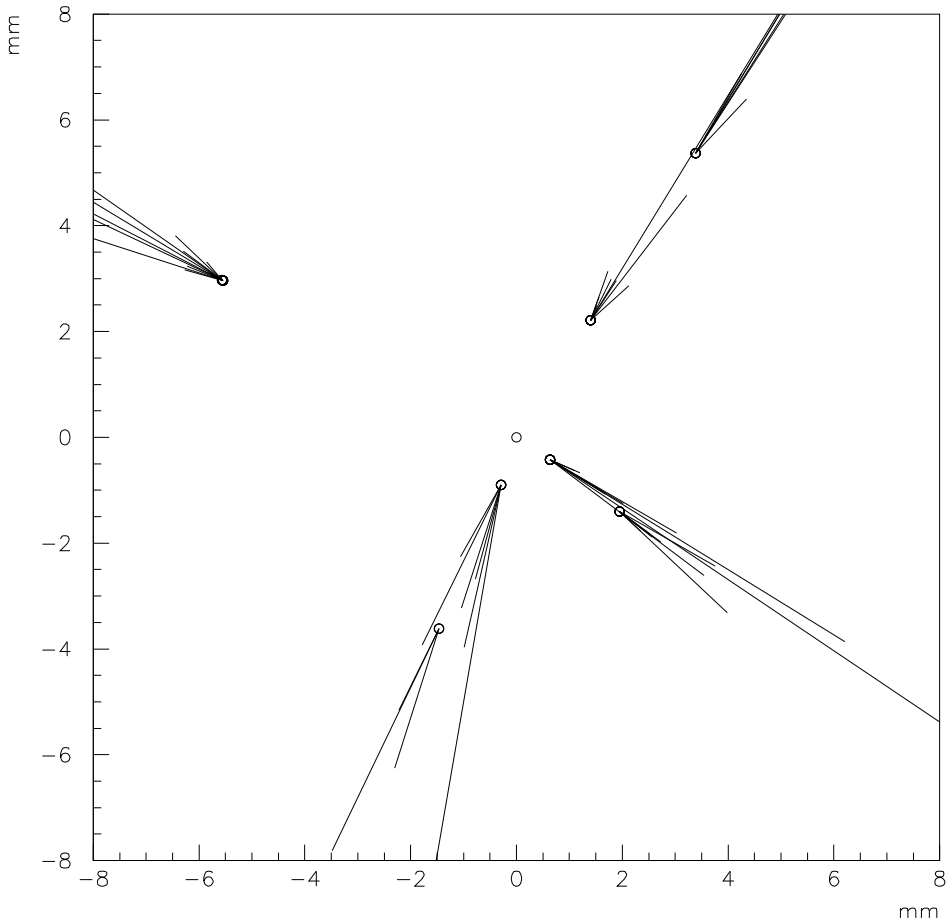

Figure 5.1: A simulated $H^0Z^0 \rightarrow b\bar{b}b\bar{b}$ event, where only the decay products of the B mesons are shown. $E_{cms} = 192$ GeV and $m_{H^0} = 80$ GeV.

Fig. 5.3 shows the energy distribution, of the same event as the one in the two previous figures, as a function of the spherical coordinates θ and ϕ, with the primary vertex at the center. Again, this turns out to be a nice event, as all jets are depositing their energies in the barrel of the detector. There are almost no

particles in the forward region. Luckily the jet from the primary vertex mixes with the jet in the upper left corner of Fig. 5.2, leaving only four well defined jets in the detector.

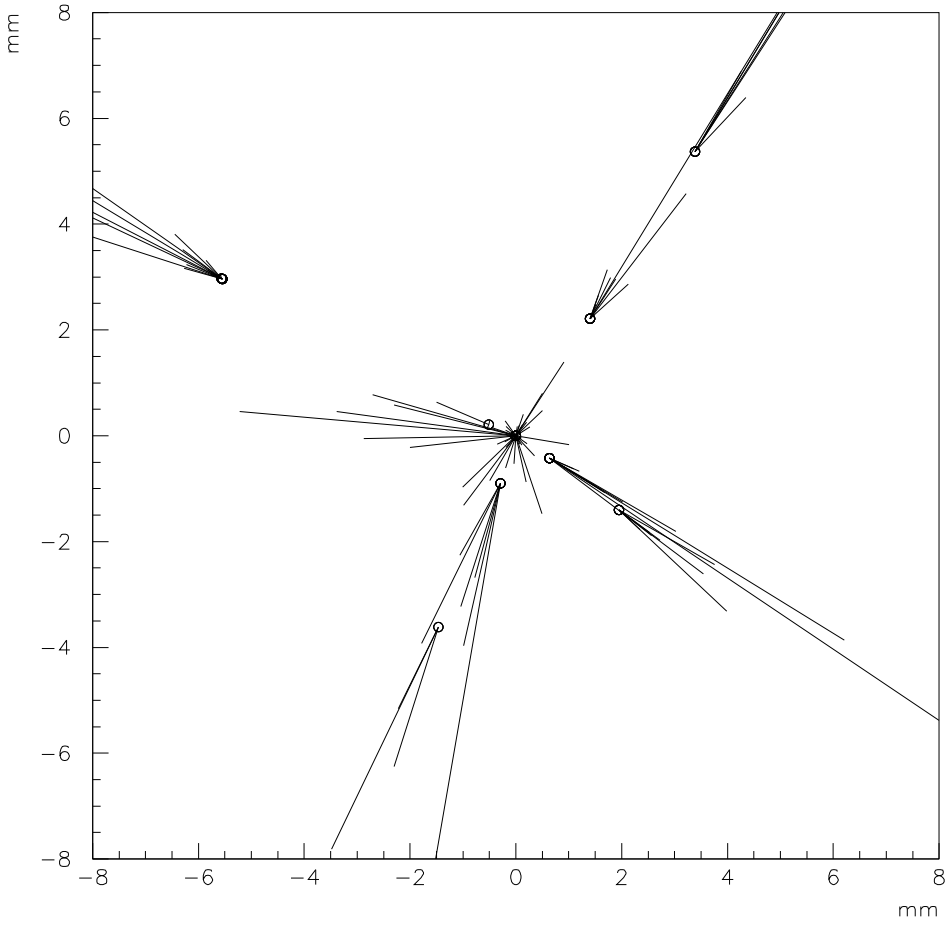

Figure 5.2: Same event as in Fig. 5.1, but with tracks of all stable particles present.

A single H^0Z^0 event has been presented, but still little has been said about the specific characteristics of Higgs events compared with the background events, described in chapter 4. As mentioned in chapter 3, the Higgs bosons have a very high rate of decay into $b\bar{b}$. At the Higgs masses obtainable at LEP200, the branching ratio of Higgs into B mesons is 87%, so looking for B mesons is obviously the best way to start the hunt. The remainder of the Higgses decay into tau leptons, charm quarks and other particles, but it is only the processes of Higgs decay into b quarks that have been studied in this thesis.

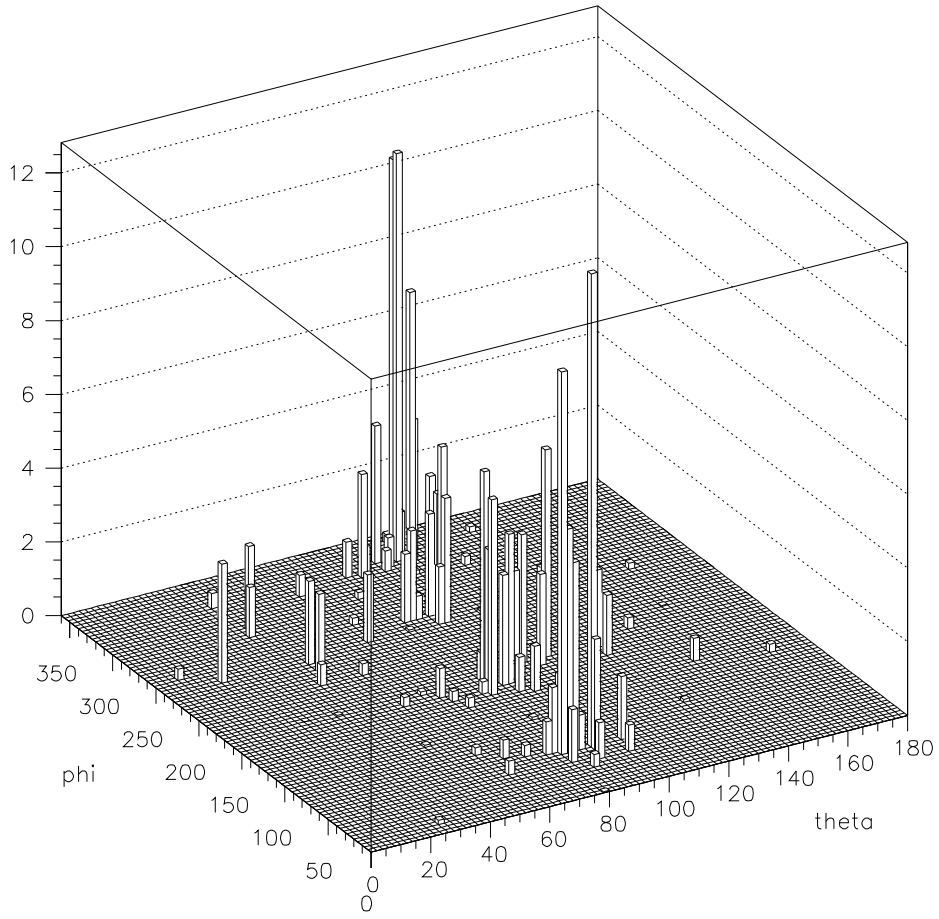

Figure 5.3: Energy distribution in the $\theta\phi$-plane, of the Higgs event displayed in Fig. 5.1 and Fig. 5.2.

Fig. 5.4 shows a simulated $h^0A^0 \rightarrow b\bar{b}b\bar{b}$ event projected onto a plane perpendicular to the beam pipe of the DELPHI detector, where h^0 and A^0 are the two lightest of the five Higgs bosons of the Minimal Supersymmetric Model. It was simulated at $E_{cms} = 192$ GeV and with h^0 and A^0 masses around 90 GeV. This $4b$ event is very similar to $4b$ events of the H^0Z^0 signal, such as the one displayed in Fig. 5.2. The three circles consisting of connected bars, or silicon detector modules, is the micro vertex detector of DELPHI. Unfortunately, the program used to display the $4b$ event extrapolates all tracks into the primary vertex, destroying the possibility to observe secondary vertices as those in Fig. 5.1 and Fig. 5.2. Secondary vertices and offsets of the tracks are however still present in the data tapes, and prove very helpful, as discussed later in this chapter.

5.3 How to find B mesons

High energy B mesons resulting from the decay of a Higgs boson typically travel a few millimeters, as Fig. 5.1 shows, before they decay into other particles. The B mesons usually decay into D mesons, which decay into K mesons, which finally decay into π mesons. This chain of decays produces a shower of stable particles, which we detect. Such showers or jets from B mesons can have a great variety in particle abundance, from just a few and up to 50 or so. Even though B jets generally have more particles than jets from lighter mesons, the particle abundance is not suited for B jet search. It turns out that jets of light mesons, often have substantial numbers of particles too, and the particle content of different kinds of jets is much too varying for any categorization of jets on that basis. It seems that the number of particles of a jet is mainly governed by the energy of its original particle, and not by its specific character.

The next step was to look at the specific particle content of different jets. The idea was to see an abundance of K mesons in B jets, because of decay of B mesons into D mesons and eventually K mesons, but this actually failed. It turned out that jets from light up and down quarks often contained several K mesons. The number of K mesons in different jet types seemed to vary randomly, even more than the number of particles. And so the K meson content of jets is possibly even worse than particle abundance in categorizing different jet types. The other particles in jets are usually π mesons and gammas of little interest. The characteristics of the B jets are not obvious to find, but there is one thing that comes to aid.

The B mesons are heavy particles, with masses around 5 GeV. As they decay, this invariant mass has to be conserved. The only way for the lighter fragments to achieve this conservation of invariant mass, is to spread out. Seen in the system of rest in the B meson reference frame, the decay fragments will spread in all directions, but in a typical laboratory setup, the B mesons will move at great speeds, leading to the formation of jets. Even though the great momentum of the

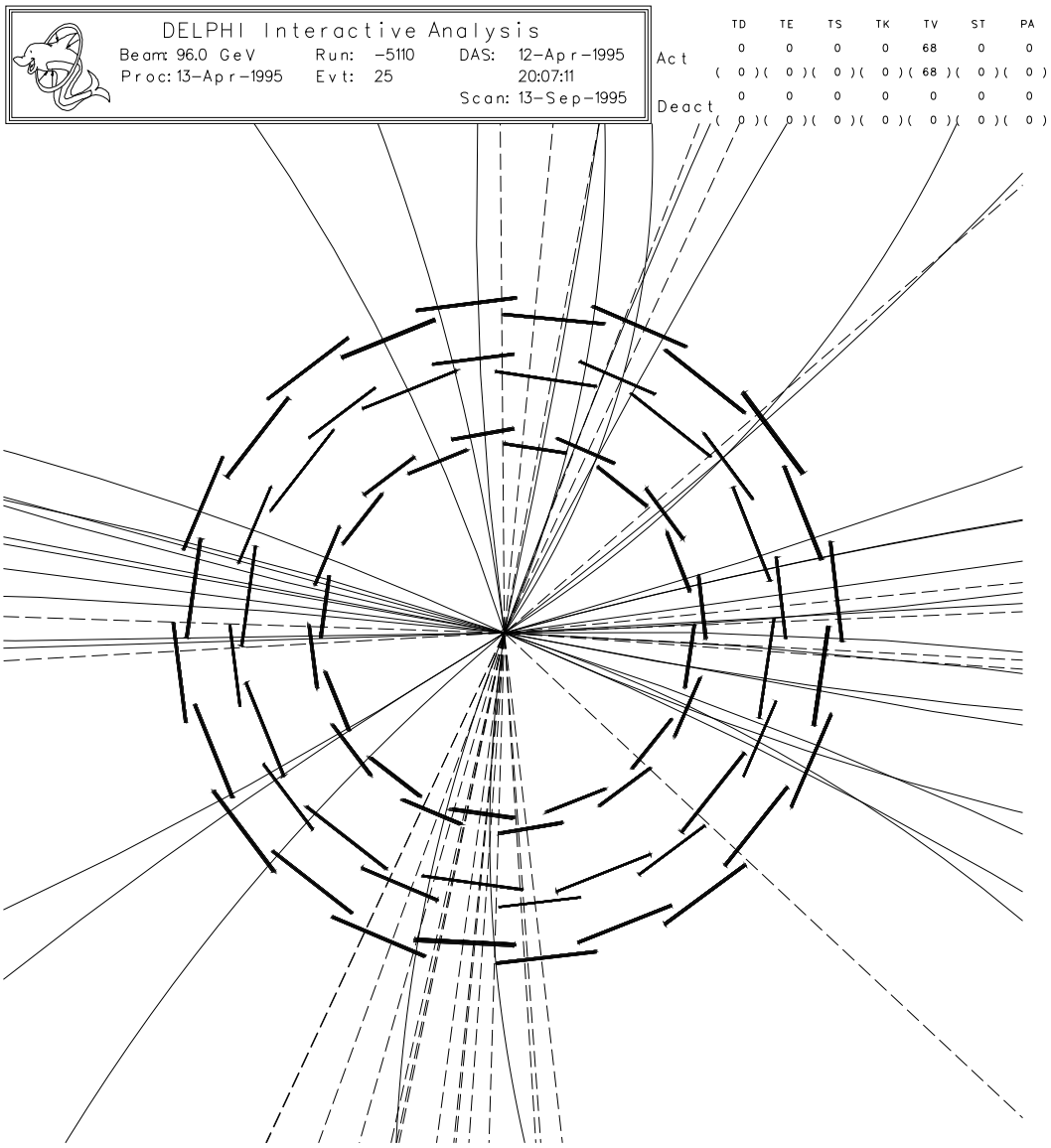

Figure 5.4: Graphical display of simulated $h^0A^0 \to b\bar{b}b\bar{b}$ event at $E_{cms} = 192$ GeV. All tracks are extrapolated into the primary vertex.

decaying B mesons somewhat blurs the small momenta of individual fragments, resulting from the decay of the B meson, the effect is still useful. Some of the B mesons decay into a muon plus hadrons. This decay mode is particularly useful, because of the high transverse momentum of the muon compared to the momentum of the associated B jet. Unfortunately, the branching ratio of this process is only 0.11, so some other identification technique is obviously needed.

Fortunately the B mesons have a relatively long lifetime, giving them a typical decay length of 3 millimeters. The great transverse momenta of the decay products of a B meson relative to the momentum of the original B meson and its decay outside of the primary vertex leads to big impact parameters of the decay products. The impact parameter of a track is defined as the distance between the primary vertex and the point of the track, closest to the primary vertex. Negative impact parameters occur when tracks are assigned to particular jets, as described below. The clustering routine LUCLUS was used to reconstruct jets. A track assigned to a particular jet, obtains a negative impact parameter if it passes behind the primary vertex, seen from the direction of the jet. Negative impact parameters should ideally not occur, but uncertainties in the measuring of impact parameters and partial mixing of different B jets, lead to such impact parameters. These effects are illustrated in Fig. 5.5, where the dotted lines are tracks assigned a negative impact parameter.

Fig. 5.6 shows the distribution of impact parameters of 20000 H^0Z^0 events, generated by PYTHIA. Almost all tracks have impact parameters above -2.0 mm and below 2.0 mm, so these numbers were chosen as natural boundaries. The actual impact parameters obtained from PYTHIA had no uncertainties, so uncertainties were added, following a Gaussian distribution of 150 micron width, to all tracks. This is somewhat worse than the actual accuracy of the micro vertex detector. The gaussian uncertainties smeared the very sharp peak at origo, obtained directly from simulations, into the relatively broad peak of the figure. The long tail of the negative impact parameters, are mainly a result of partial mixing of jets as Fig. 5.5 shows. The figure obviously has a great abundance of positive impact parameters, which is of course expected, as almost all H^0Z^0 events contain B jets. D jets too, have an abundance of positive impact parameters, though not as many or as large as those from B jets. Impact parameter distributions of events without any B or D jets are almost symmetric, with only small tails on both sides of the central peak.

5.4 The B tagging procedure

The trick is to decide whether a particular track is actually from the primary vertex or not. This is not simply stated as a yes or no, but as a probability ranging from zero to one. Such a probability should depend on the measured impact parameter of a track and the distribution of tracks that actually had zero

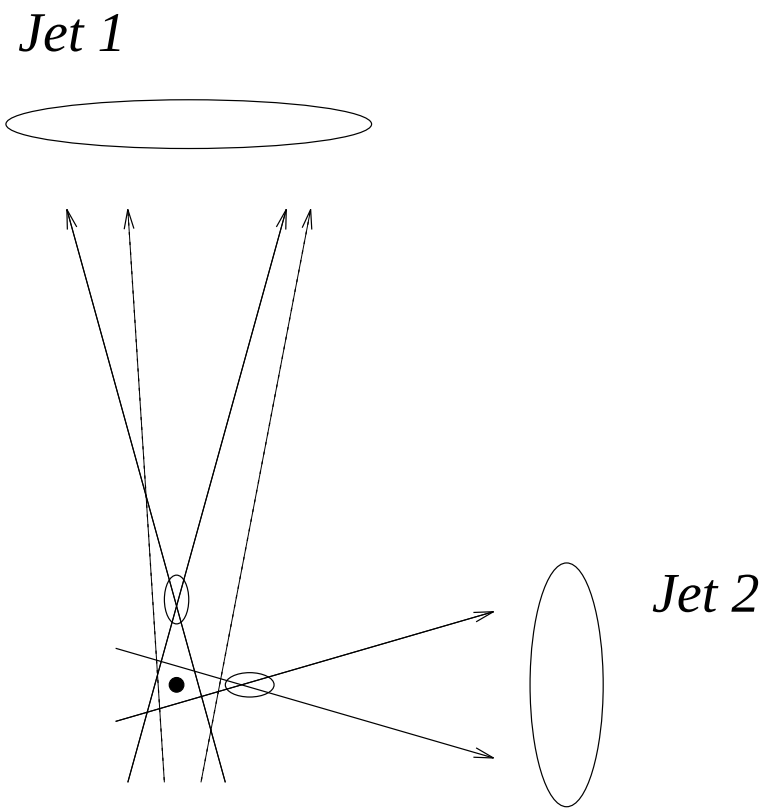

Figure 5.5: Illustration of how the sign of the impact parameter is defined. Dotted tracks are assigned a negative impact parameter. The primary vertex is denoted by a black dot, and secondary vertices are denoted by small ellipsoids. Note how one of the dotted tracks is assigned to a wrong jet, while the other gets a negative impact parameter because of bad track reconstruction.

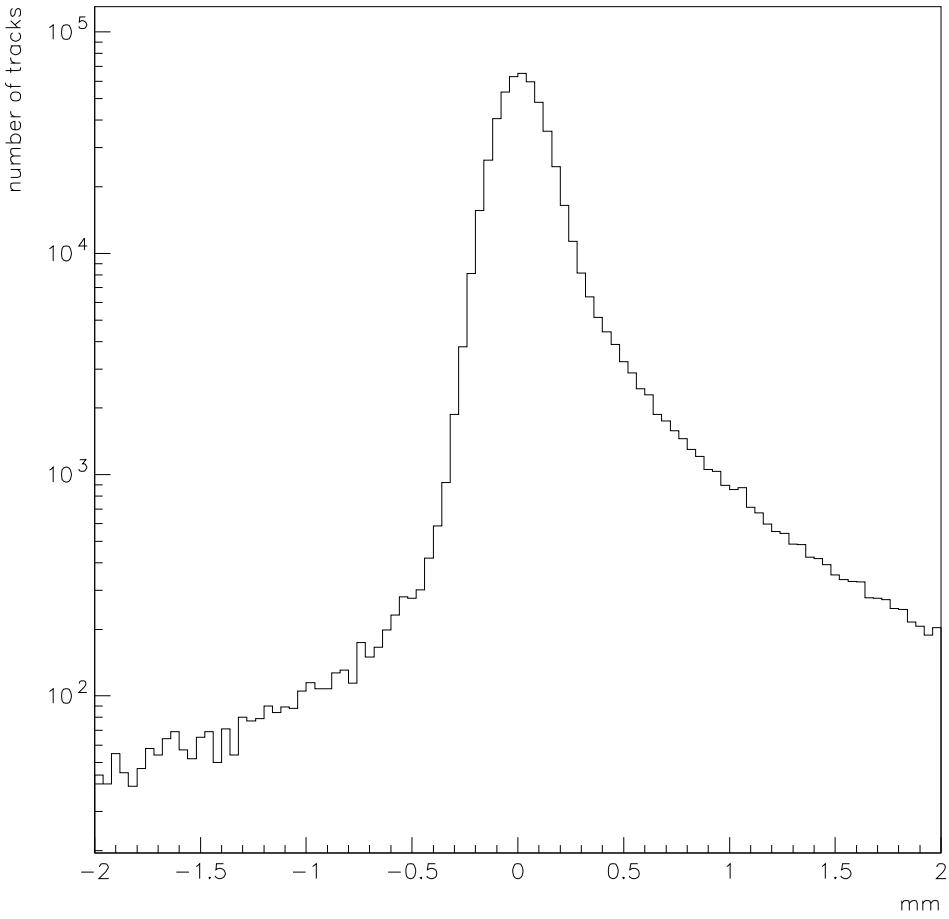

Figure 5.6: Impact parameters of all tracks in 20000 H^0Z^0 events.

impact parameter originally.

It was decided that the probability, or positive track probability, should be defined as an integral of a normalized function closely resembling the impact parameter distribution of tracks that originally had impact parameters of zero. Such a normalized function is called a resolution function. The distribution of negative impact parameters in Fig. 5.6 is thought to closely resemble the distribution of positive impact parameters if no B or D jets were present, hence if all tracks were originally from the primary vertex, this can be used to find the resolution function, as Fig. 5.7 shows.

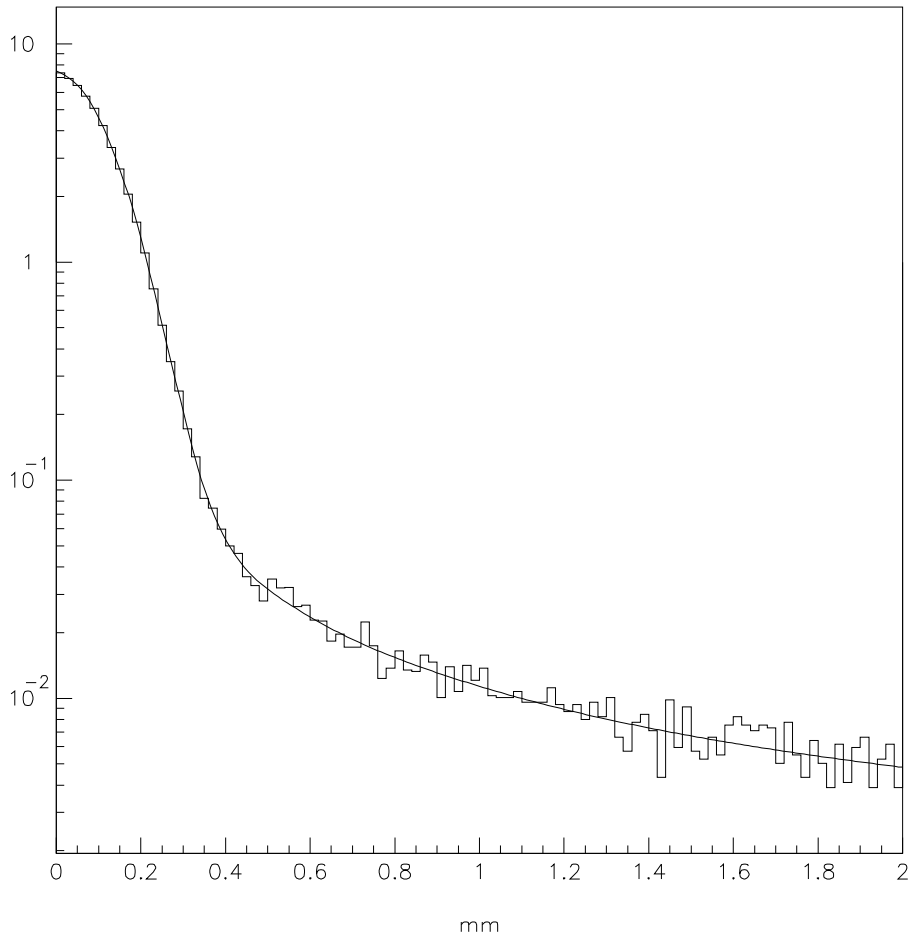

Figure 5.7: Negative impact parameters with a resolution function fit.

Now, the idea is to pick the measured positive impact parameter of a track and do an integral of the resolution function from the measured impact parameter to the boundary at 2.0 mm. The tracks with very small positive impact

parameters get a track probability very close to one, because the integration of the resolution function is done almost along the entire interval of the function. The normalization of the function secures the fact that a track with an impact parameter of zero ought to have a track probability of exactly one. This means that the track is thought to come exactly from the primary vertex.

On the other hand, tracks with positive impact parameters close to 2.0 mm, get a very small track probability, because of the slim tail of the resolution function. This means that these tracks are given a very small chance that they actually came from the primary vertex. This is where we hope to find our tracks from B jets. In this process of probability calculations, only the positive impact parameters between 0.0 and 2.0 mm are used, because this is where the interesting impact parameters of B jets are found.

The individual track probabilities of each track have been defined, but a single probability of an entire event is needed. It was suggested by Brown[13] that such a N-track probability should be defined as a weighted product of the individual track probabilities of the event in the following way

$$P_N \equiv \Pi \cdot \sum_{j=0}^{N-1} \frac{(-ln\Pi)^j}{j!}$$

where

$$\Pi \equiv \prod_{i=1}^{N} P(s_i)$$

and $P(s_i)$ are the individual track probabilities. This formula turns out to be well suited for our purpose. The N-track probability, P_N, is ranging from zero to one, as it ought to, and it is not sensitive to the number of tracks in an event, only to the magnitude of the individual track probabilities. Many track probabilities close to one, ie. there is a great chance that the tracks are originally from the primary vertex, leads to a N-track probability close to one. This means that the event is likely not to be a B jet event, while a very small N-track probability indicates a B jet event. The N-track probability is a continuous parameter, which implies that the purity and efficiency of a sample containing B jets, can be tuned exactly for our needs. A tight cut, very close to zero, generates a pure sample, containing mainly B events, but many B events are lost in the process and the efficiency drops. If, on the other hand, a loose cut is made, we will keep most of the B events in the sample, and thereby obtain a high efficiency, but the purity drops, as we introduce more new background than new B events into the sample.

Fig. 5.8 shows the N-track probability distribution of 20000 H^0Z^0 events. The sample obviously contains many B events, as the very high peak at zero shows. In comparison, the distribution of a sample without any B or D events is ideally flat, because of the specific B tagging procedure, though it usually got a small peak at zero or one, depending on the quality of the calibration of the resolution function.

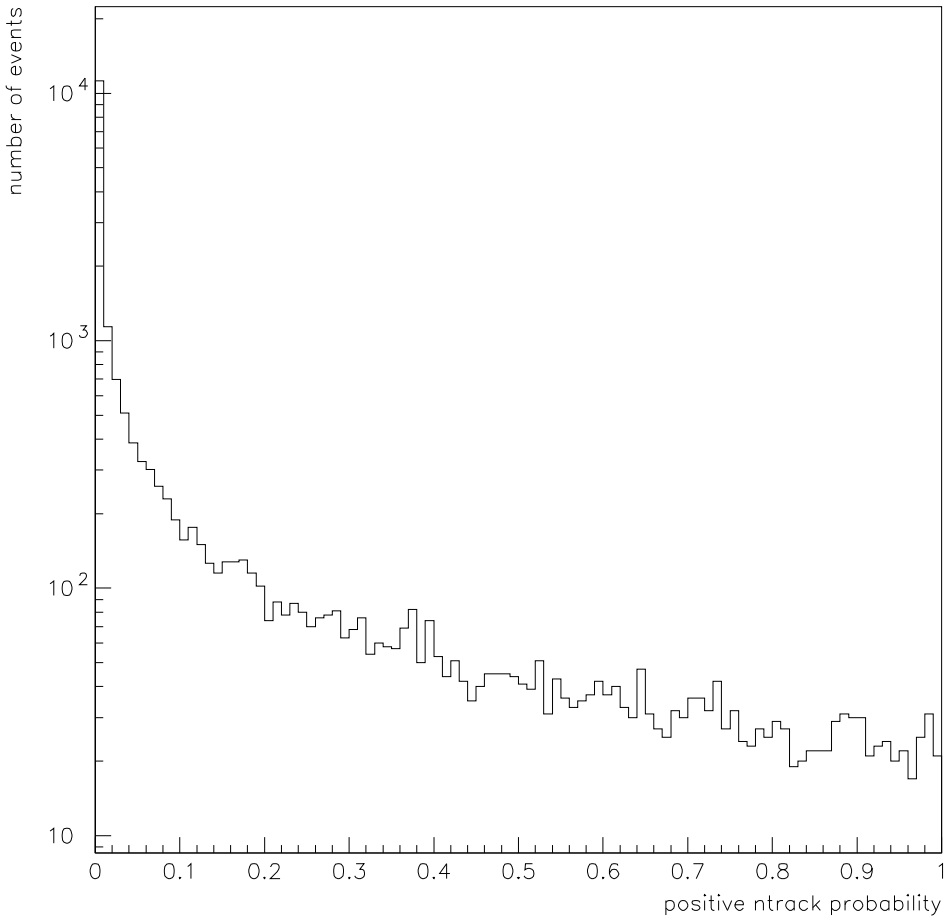

Figure 5.8: Positive N-track probabilities of 20000 H^0Z^0 events.

The discussion in this chapter has only concerned general aspects of the Higgs events so far, and only events simulated by PYTHIA have been studied. These basic simulations are naturally obsolete, and much more thorough and detailed simulations are needed. Such full simulations are performed by a program called DELSIM, which is continuously developed, to account for characteristics of new detectors and more detailed physics analysis. It would be far out of the scope of this thesis to describe in detail how this simulation program works but the basic lines can be drawn. First, a basic event is generated using PYTHIA and JETSET. Each track of the generated event is then guided through the detector to simulate its detector response. This is a very complicated process that has to take many factors into account. The effect of the magnetic field has to be calculated, and every time a particle passes through regions of dense matter, energy loss and secondary interactions have to be considered. DELSIM also simulates how the different detectors respond to a given particle. The particle may pass through a detector module, depositing most of its energy or perhaps nothing! Such random behavior, that is exhibited by most particles running through the detector, also has to be simulated in a correct way. After this comprehensive and computer power consuming process the DELSIM results are finally analysed by DELANA[14] to obtain the full Data Summary Tape format (DST[15] format), which was used in this analysis. DELANA is also used for analyzing the detector readout of real events. The program uses all the acquired data from the DELPHI detector, or from DELSIM, to reconstruct tracks and momenta of the original particles in a given event.

This chapter has considered broad aspects of Higgs events, but the next chapter will consider much more specific characteristics of these events and only of the neutrino channel, ie. only Higgs events where the Z^0 decays into two neutrinos and the Higgs boson decays into $b\bar{b}$, have been studied.

Chapter 6

Optimization of event selection based on full simulations

6.1 Characteristics used for event selection

This chapter explains the various characteristics used for selecting events in the neutrino channel, $e^+e^- \rightarrow H^0\nu\bar{\nu}$, of the Higgs process, and presents figures to show exactly how distributions of each characteristic are cut and the effect on both signal and each of the most important backgrounds. Each cut has been carefully chosen to select Higgs events of the neutrino channel with high efficiency while reducing the background to an acceptable level. The characteristics that will be used for event selection are the following;

- Number of jets, as reconstructed by LUCLUS.
- Angle between total momentum and the beam pipe.
- Acoplanarity of events.
- Total visible energy of events.
- Energy deposited in the STIC, the HPC and the FEMC sub-detectors of DELPHI.
- The N-track probability, found using the B tagging procedure explained in the previous chapter.
- A graphical cut in total momentum versus acolinearity.
- And finally the charge generated in the 40° taggers.

All figures in this chapter are made using simulations at $E_{cms} = 192$ GeV, and $m_{H^0} = 90$ GeV, unless otherwise stated. 192 GeV is the maximum energy that will be obtained at LEP200, and hence the most interesting to study in detail. The final upgrade of LEP to 192 GeV will occur in May 1998.

6.2 Number of jets

The Higgs signal studied in this thesis, is the part of the H^0Z^0 signal where $Z^0 \rightarrow \nu\bar{\nu}$ and $H^0 \rightarrow b\bar{b}$. This means that the sought Higgs events only contain two jets, the two B jets. The B jets have a strong tendency of breaking up into small jets, but this can to some extent be accounted for by allowing a large d_{join} parameter when using LUCLUS, as described below. The d_{join} parameter essentially describes how far, in transverse momentum, two particles can be from each other before they are joined into one jet by LUCLUS. If the parameter is set to a small value, say 1 GeV, the clustering routine will only join particles that are very near in momentum into clusters, and many small clusters will be the result. If on the other hand, 10 GeV is used for the d_{join} parameter, things will

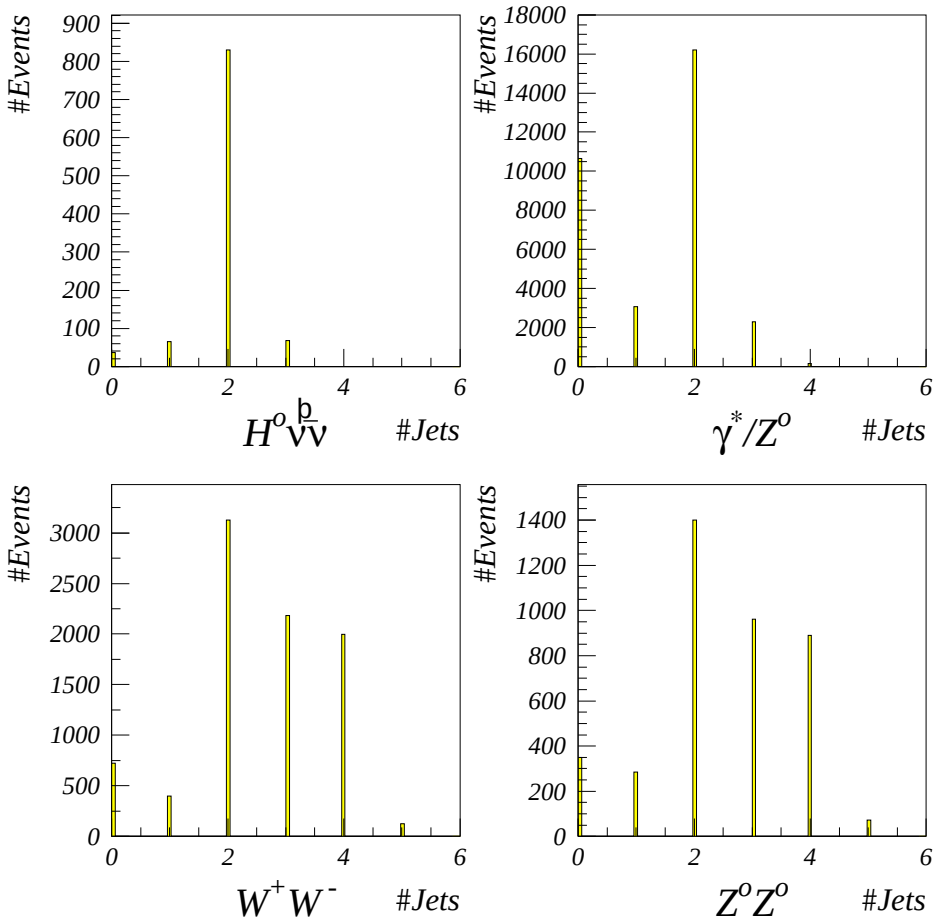

Figure 6.1: Number of jets reconstructed by LUCLUS. $E_{cms} = 192$ GeV and $m_{H^0} = 90$ GeV.

look different and the various small clusters are joined into a few big ones. The usual values for d_{join} which have been used for reconstructing clusters at LEP is 3-4 GeV, while this analysis was made with the relatively big value of 10 GeV.

Fig. 6.1 shows the number of jets reconstructed by LUCLUS using $d_{join} = 10$ GeV. In addition it was required that each jet had more than 10 GeV of visible energy and more than four tracks. These extra conditions were adopted to ignore jets that consist of one or just a few tracks, and jets of very low energy. These jets are of little interest and unlikely B jets. The simulated data contain many events with no tracks at all. These are mostly $\gamma^\star/Z^0$ events where initial state radiation photons travel down the beam pipe and the Z^0 decays into two neutrinos. To keep things tidy and avoid annoying empty events in the figures, events with less than two jets have been left out of all further figures in this chapter.

It is clear that a great majority of the Higgs neutrino events have two well defined jets as expected. Most of these are B jets. The $\gamma^\star/Z^0$ background also has an abundance of two-jet events, as the Z^0 usually decays into two quarks. The other two background processes W^+W^- and Z^0Z^0 also have an abundance of two jets but these also have considerable amounts of events with three or four jets. The four-jet events of the W^+W^- process are mainly a result of both W bosons decaying into two quarks, while the four-jet events of the Z^0Z^0 process occur when both Z^0 bosons decay into quarks or leptons.

Demanding two jets in the candidate Higgs events not only serves to remove some background events, but the stage is also set for clean calculation of other characteristics such as acoplanarity and acolinearity.

6.3 Angle between total momentum and beam pipe

The momenta of all visible tracks in the event are summed to find the total momentum of the event. The total momentum is ideally supposed to be zero as the momentum was before the e^+e^- interaction, but all particles are capable of avoiding detection, either because of their non-interactive nature or because of cracks and holes in the detector. The holes in the detector along the beam pipe are of particular importance when considering the $\gamma^\star/Z^0$ background, because the initial state radiation photon, resulting from radiative return to Z^0, usually is emitted along the beam pipe. This leads to large missing momenta, or equivalently, large visible total momenta. These visible total momenta of the $\gamma^\star/Z^0$ events are also pointing along the beam pipe but in the opposite direction of the escaping photons. This is illustrated in Fig. 6.3.

Fig. 6.2 shows exactly this behavior. The figure, again at 192 GeV, and only with events of at least two jets, displays the angle between the total visible momentum and the beam pipe. All momenta are rather equally distributed

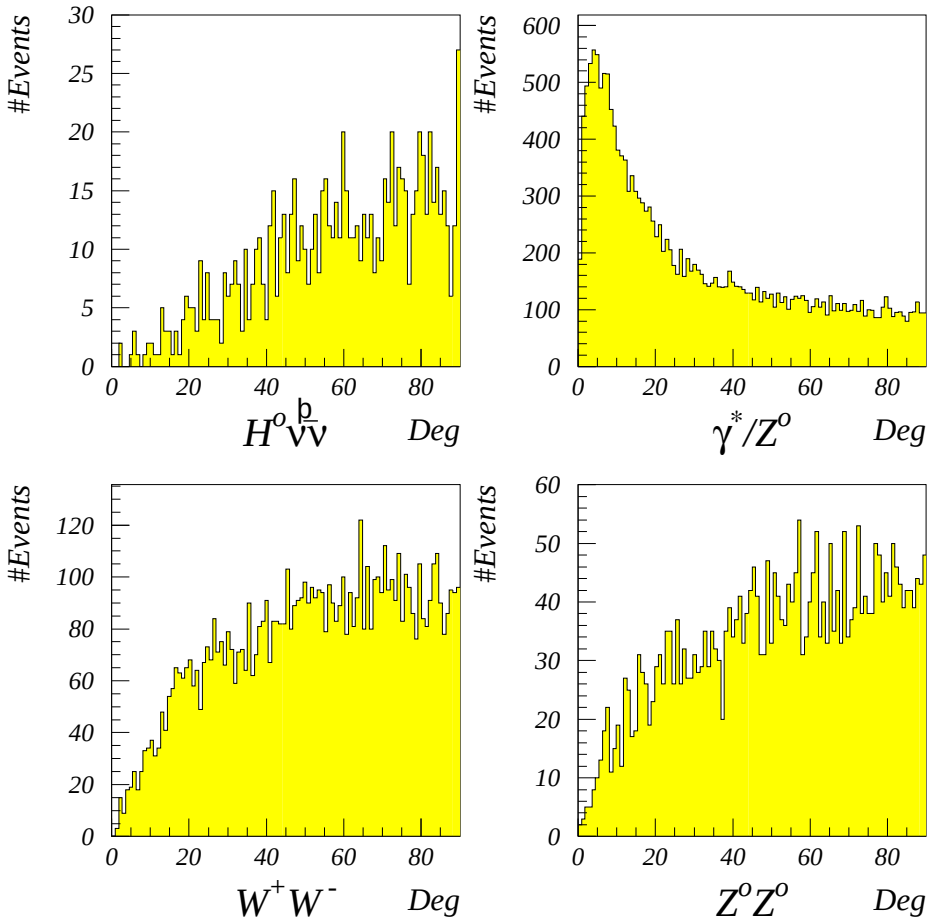

Figure 6.2: Angle between total momentum and beam pipe. $E_{cms} = 192$ GeV and $m_{H^0} = 90$ GeV.

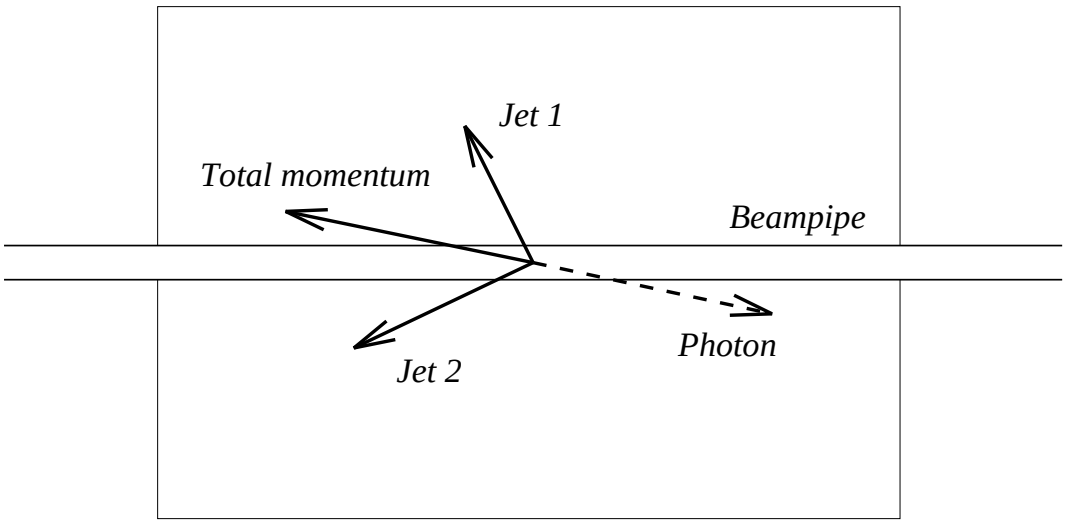

Figure 6.3: Illustration of the total momentum of a γ^*/Z^0 event where the initial state radiation photon, from radiative return to Z^0, escapes down the beam pipe.

in space except the γ^*/Z^0 momenta which has a very strong bias towards the beam pipe direction. A cut at 27 degrees is very effective in reducing the γ^*/Z^0 background while only a small portion of the Higgs signal is removed. This cut is designed for the γ^*/Z^0 background, so it doesn't do much for the W^+W^- and Z^0Z^0 backgrounds.

The direction of the momenta has proven useful, but the magnitude of the momenta also promise progress. There is a significant correlation between the magnitude of the total momentum, of each event, and the corresponding acolinearity of the same event. This makes it profitable to construct a graphical cut in magnitude of total momentum versus acolinearity. Such two-dimensional scatter plots are presented for all three energies, 175, 192, and 205 GeV, later. The next characteristic to be studied also relates to the γ^*/Z^0 background in particular. This is the acoplanarity.

6.4 Acoplanarity of events

The cut in acoplanarity is certainly one of the most important in the entire analysis. To calculate acoplanarities it's necessary to define a plane which acoplanarity angles are relative to. In this thesis the preferred plane was the one spanned by the most energetic of the two jets and the beam pipe. Recall that events with two jets have been selected. The acoplanarity is then defined as the angle between the second jet and the plane of the most energetic jet and the beam pipe. This is illustrated in Fig. 6.5 where both the $H^0\nu\bar{\nu}$ signal and the important γ^*/Z^0 back-

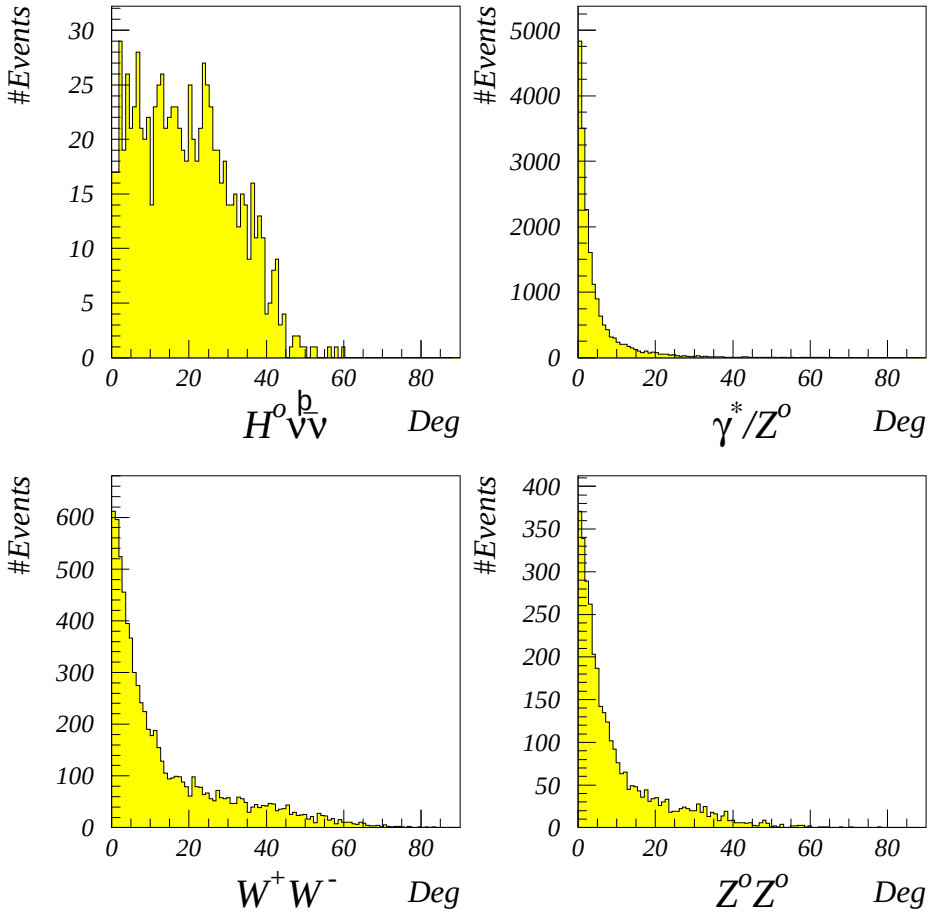

Figure 6.4: Acoplanarity of events. $E_{cms} = 192$ GeV and $m_{H^0} = 90$ GeV.

ground are displayed. The figure illustrates how the rather broad distribution of acoplanarities of the signal events, shown in Fig. 6.4, is obtained. The very narrow peak of the acoplanarity, at zero, for the γ^*/Z^0 background also finds its explanation in the illustration. As pointed out above, when studying the angle between the total momentum and the beam pipe, the initial state radiation photons, from radiative return to Z^0, are usually emitted in the direction of the beam pipe. This leads to a much more bound configuration for the γ^*/Z^0 background than for the signal events. As an initial state radiation photon travels down the beam pipe, the conservation of momentum forces the momenta of the two jets from the decayed Z^0, and the momentum of the escaping photon to constitute a plane. This means that the two jets and the beam pipe are forced to constitute a single plane, thereby limiting the acoplanarity of events to a very narrow peak. This is certainly not the case with the signal events, as the two neutrinos from the decayed Z^0 of the H^0Z^0 signal are free to escape, with much of the momentum, in any direction.

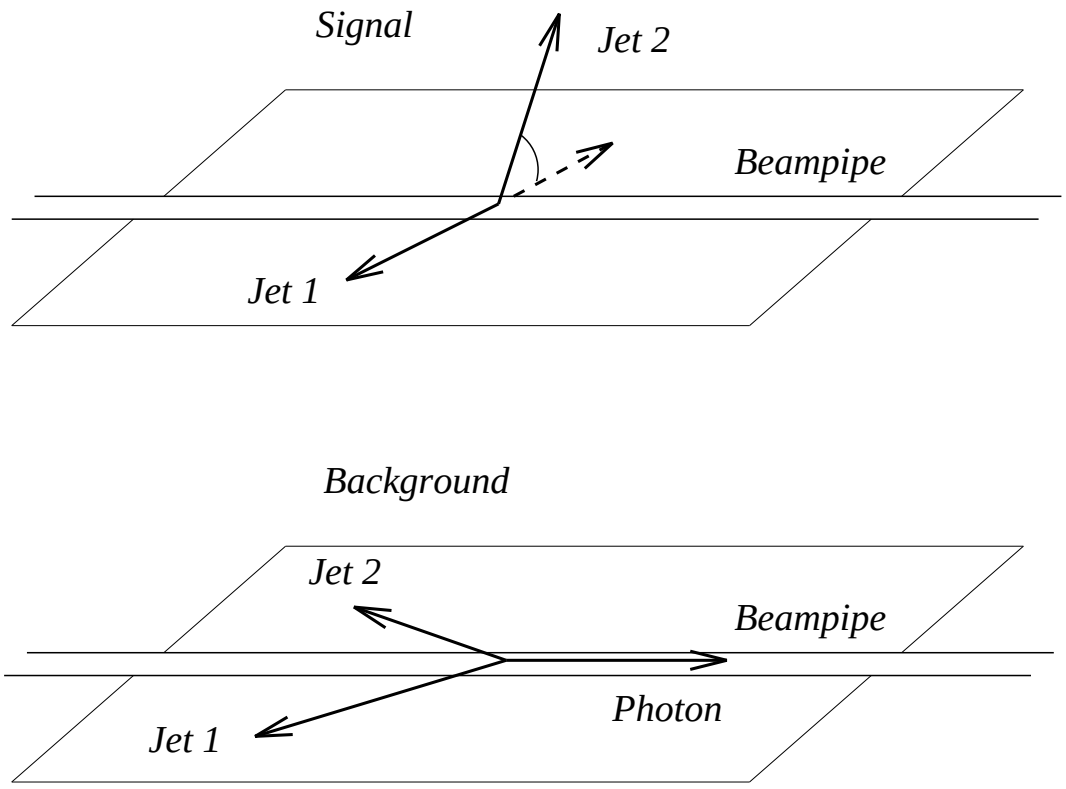

Figure 6.5: Illustration of the acoplanarity of both the $H^0\nu\bar{\nu}$ signal and the γ^*/Z^0 background. The powerful initial state radiation photon heading down the beam pipe, locks the two jets of the γ^*/Z^0 background into a configuration of minimal acoplanarity.

Fig. 6.4 displays the acoplanarities of the different processes. The acoplanari-

ties were calculated based on jet reconstruction by LUCLUS. A cut at 7° turned out to be most profitable. This leaves only the small tail of the γ^*/Z^0 background while most of the signal survives. The cut was carefully chosen at 7°, to avoid too much impact on the signal yet cutting most of the background.

6.5 Visible Energy in the detector

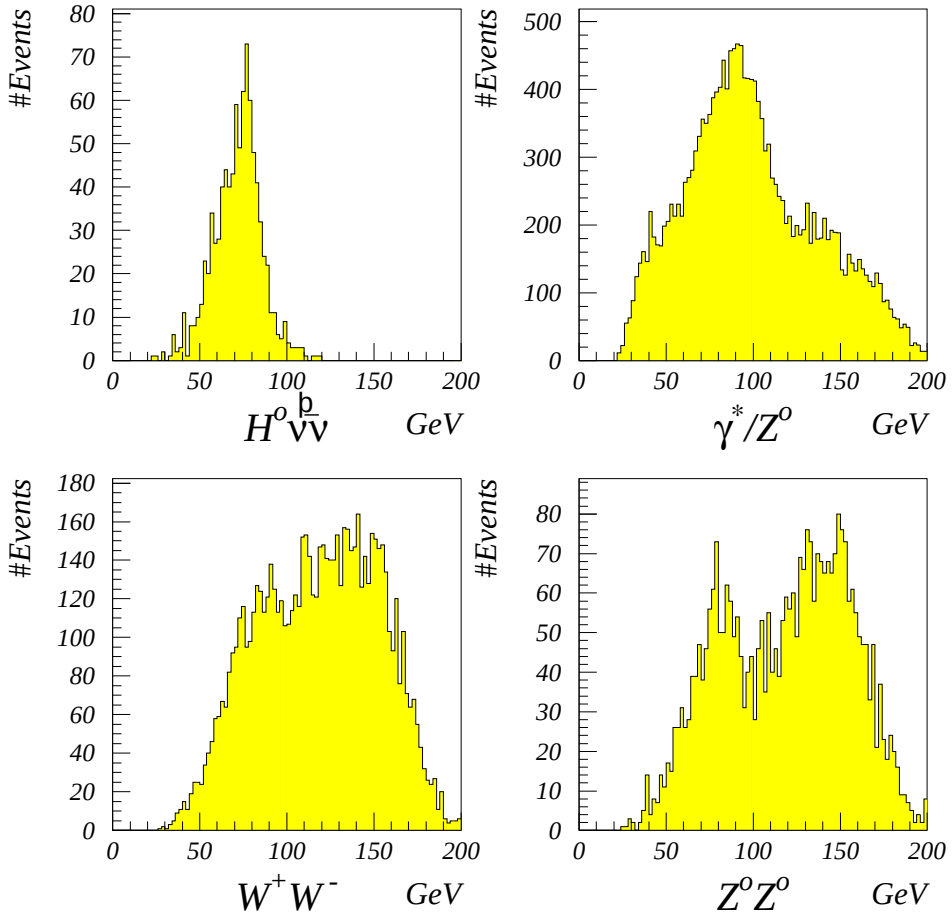

Figure 6.6: Visible energy of events. $E_{cms} = 192$ GeV and $m_{H^0} = 90$ GeV.

After studying some cuts especially aimed at removing the $\gamma^\star/Z^0$ background, attention is put on energy deposits in various parts of the DELPHI detector. The total visible energy of events, at a center of mass energy of 192 GeV as in the previous figures, is shown in Fig. 6.6. It is immediately clear that the two neutrinos of the $H^0\nu\bar{\nu}$ signal escape with almost half of the available energy, leaving the signal events below 100 GeV. A cut at 95 GeV was chosen, leaving most of the signal events untouched, while particularly the W^+W^- background suffers great reduction. The energy distribution of the $\gamma^\star/Z^0$ background is roughly resembling two super positioned distributions, one for events from radiative return to Z^0, and one for events without any powerful initial state radiation. The distribution of the dangerous events from radiative return to Z^0, is peaked at around 90 GeV, while the other distribution is peaked at much higher energies, probably $\sim$130 GeV. This means that a selection of events with less than 95 GeV energy will remove most of the $\gamma^\star/Z^0$ events without powerful initial state radiation, while most of the dangerous events from radiative return to Z^0 will survive. In addition it was decided that the visible energy is also supposed to be higher than 35 GeV. This cut has no impact on the signal, and only barely scratches the backgrounds. It is just meant as a precaution to avoid $(e^+e^-)f\bar{f}$ events, beam-gas events, and other backgrounds of very low energy.

6.6 Energy in the STIC

Looking at the entire visible energy in the detector is useful, but it turns out that a more detailed study of the energy depositions promise further progress. As mentioned previously, $\sim$75% of the $\gamma^\star/Z^0$ events, radiate a very powerful photon in the direction of the beam pipe. Being emitted at a very low angle, the photon exits through the beam pipe out of reach of the detector. However it happens quite often that the photon enters the low angle STIC calorimeter. Fig. 6.7 shows the sum of the energies deposited in both STIC calorimeters, one for each side of the detector, using a logarithmic scale. Few of the signal events deposit more than 1 GeV of energy in both STICs, and so it was decided that no more than 1 GeV of energy deposited in the STIC calorimeters should be allowed. This removes some of the $\gamma^\star/Z^0$ background and only very little of the signal. Trying to decide exactly which type of particles that have entered the STIC is possible, but not necessary. As soon as clusters of high energy appear in the STIC, the event is cut, whether the cluster was a result of a high energy electron, a photon or something else. This is done to remove events where a powerful photon pair produces electrons that enter the STIC. The STIC is the best suited detector module for full or partial detection of photons from radiative return to Z^0, as the photons are emitted at very low incident angles. However the forward electromagnetic calorimeter, or FEMC, is also useful.

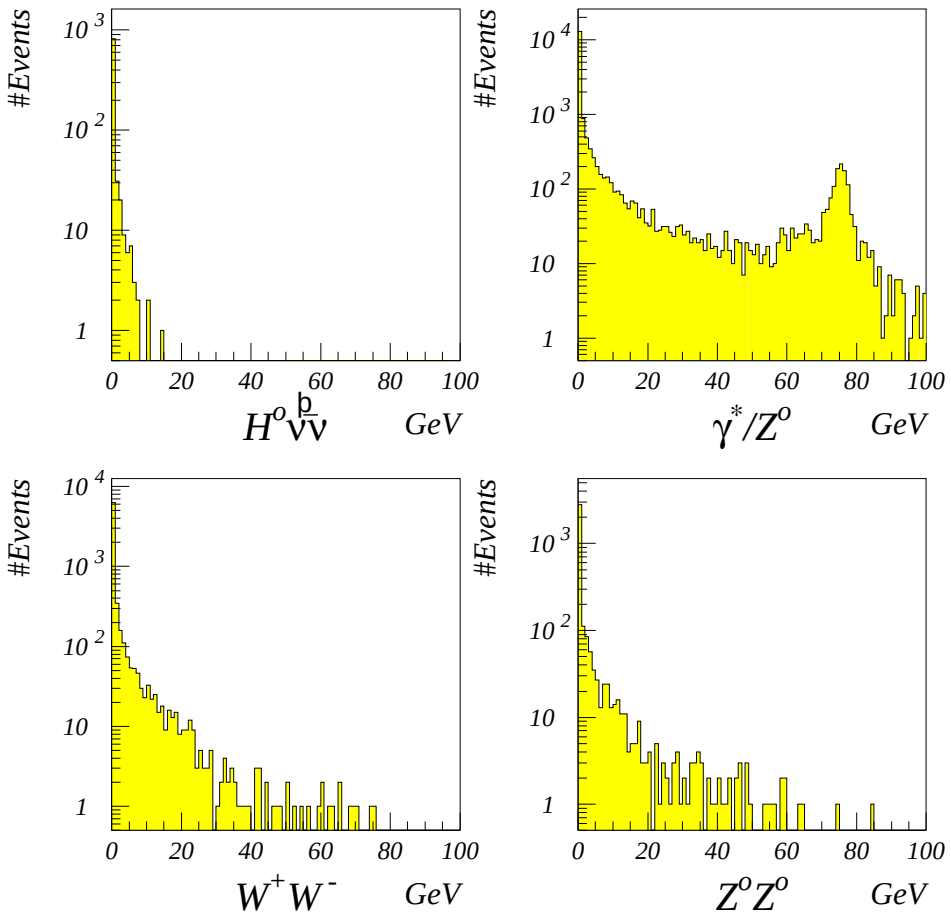

Figure 6.7: Total energy deposited in the STIC calorimeters. $E_{cms} = 192$ GeV and $m_{H^0} = 90$ GeV.

6.7 Energy clusters in the FEMC

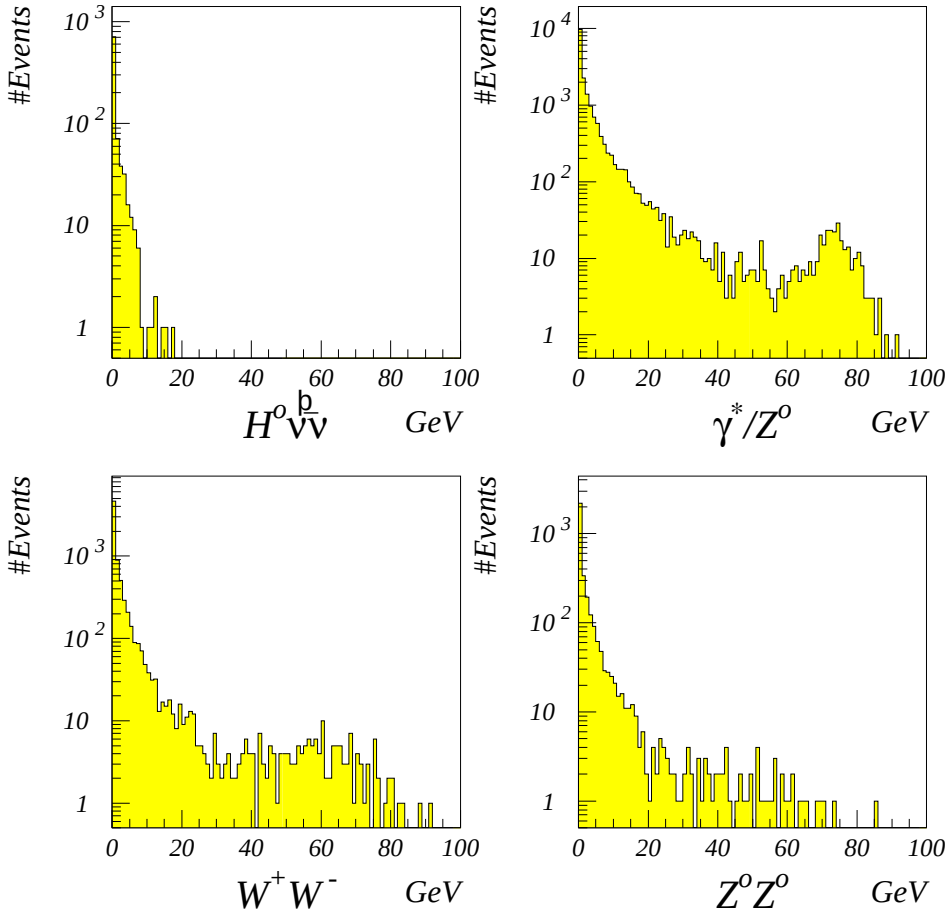

Figure 6.8: Most energetic cluster deposited in the FEMC. $E_{cms} = 192$ GeV and $m_{H^0} = 90$ GeV.

Although a bit too far from the beam pipe to detect as many initial state radiation photons from radiative return to Z^0, as the STIC, the FEMC is still useful. As Fig. 6.8 shows, using a logarithmic scale, the jets of the signal process seldom hit the Forward Electro-Magnetic Calorimeter, or FEMC. Fig. 6.7 displays the entire energy deposited in both STIC calorimeters, while Fig. 6.8 only displays the most energetic cluster or track deposited in any of the two FEMC calorimeters. Selecting events with clusters of less than 5 GeV in the FEMC, turned out nice, not doing much to the background though, but it helps. A similar selection using the High density Projection Chamber, or HPC, was done.

6.8 Energy clusters in the HPC

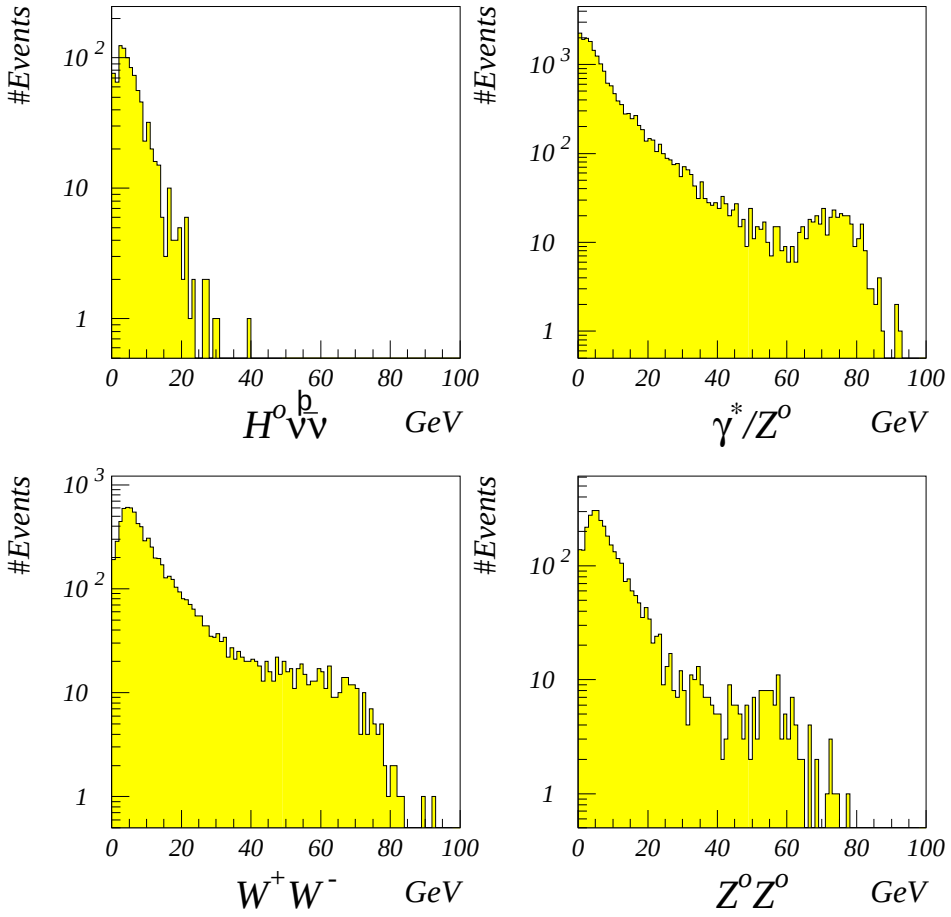

Figure 6.9: Most energetic cluster deposited in the HPC. $E_{cms} = 192$ GeV and $m_{H^0} = 90$ GeV.

This characteristic is exactly similar to the previous in the FEMC calorimeter. It's aimed at removing γ^*/Z^0 events where the photon, coming from radiative return to Z^0, hits the barrel section of the detector and is converted into electrons that are detected in the High density Projection Chamber, or HPC. These events are few but very important to remove, because they are the ones that looks most like potential Higgs events. The reason is that most of the cuts aimed especially at the γ^*/Z^0 events are based on the assumption that the photon, from radiative return to Z^0, escapes through the beam pipe, leaving powerful constraints on the two jets from the decaying Z^0. These constraints, such as minimal acoplanarity

and small angle between beam pipe and total momentum, do not apply if the photon escapes through a crack in the barrel region of the detector. The HPC luckily handles most of these dangerous γ^*/Z^0 events.

Fig. 6.9 shows the energy of the most energetic cluster deposited in the HPC, again using a logarithmic scale. Since the HPC is situated in the barrel region it usually gets hit by one or both jets of a potential Higgs event. The jets contain several high energy tracks that often deposit considerable amounts of energy in the HPC calorimeter. A low cut in energy as those applied to the STIC and the FEMC, would totally ruin the signal, so a cut at 17 GeV was chosen. It's not as tight as the FEMC and STIC cuts but it is still capable of removing the obvious γ^*/Z^0 events at least. The next characteristic to study is impact parameters and B tagging as thoroughly explained in the previous chapter.

6.9 B tagging the events

Finally comes the much awaited B tagging procedure. This was done by using the B tagging program called AABTAG[16] especially designed for the DELPHI detector. The program uses exactly the same method as the one explained in the previous chapter. A resolution function fitted for the high energy runs of LEP, was used to calculate the N-track probabilities. This probability, ranging from zero to one, indicates whether the selected event contains B jets or not. A probability close to zero means that the event is likely to have at least one B jet, while a probability considerably greater than zero or close to one means that the event is probably without B jets. Events containing jets coming from charm quarks also have a tendency of getting N-track probabilities close to zero, but these probabilities are usually not as low as those for events with B jets.

Fig. 6.10 shows the N-track probabilities calculated by AABTAG, using a logarithmic scale. Events with N-track probabilities of less than 0.001 are selected. This is a very effective selection, removing almost all the W^+W^- events, and most of the γ^*/Z^0 and Z^0Z^0 events. The selection is particularly hard on W^+W^- events as these contain very few B jets. The great majority of initial quarks from decaying W bosons are either u and d quarks, or s and c quarks. This leaves the W^+W^- events almost free of b quarks and hence free of B jets. Unfortunately, the other two backgrounds, γ^*/Z^0 and Z^0Z^0, have much more B jets from decayed Z^0 bosons. The cut however removes most of the γ^*/Z^0 and Z^0Z^0 events that don't have any B jets, and these are the great majority, as only 15% of the Z^0 bosons decay into two b quarks. The selection is hard on the signal too, removing a considerable amount of events, but it's absolutely vital in limiting the backgrounds to acceptable levels. Figure 6.11 has been added to zoom in on the range in which the selection cut is done.

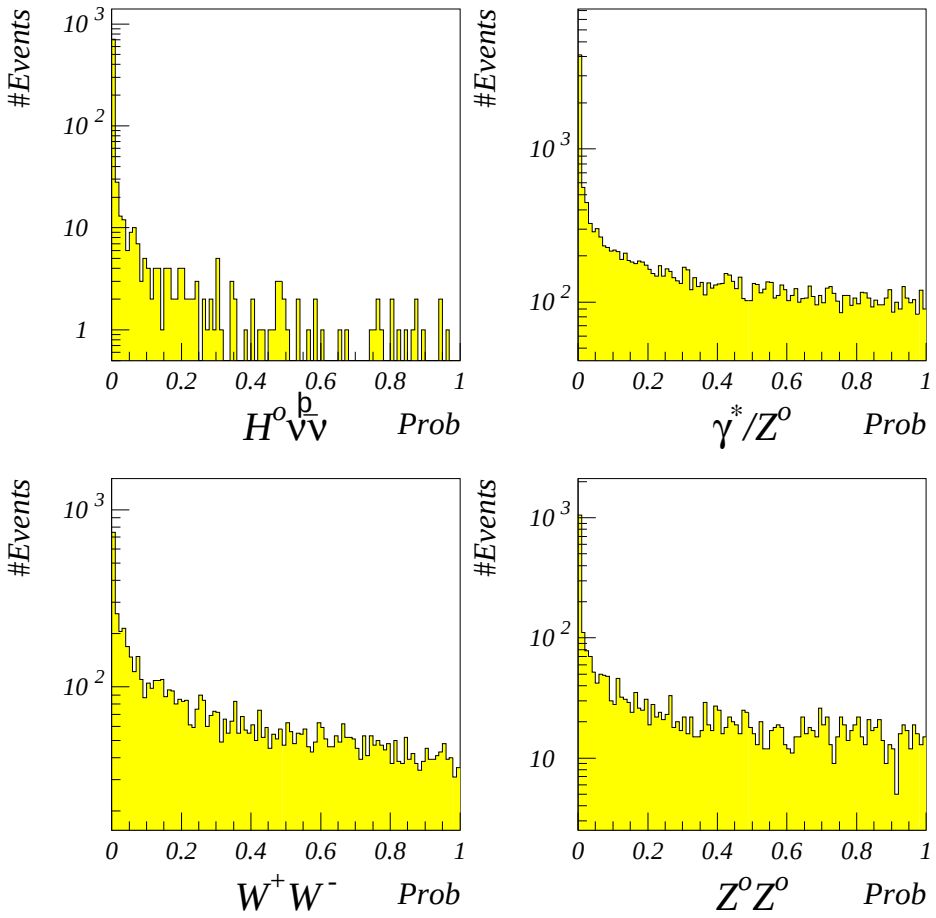

Figure 6.10: Positive N-track probabilities calculated using AABTAG. E_{cms} = 192 GeV and $m_{H^o} = 90$ GeV.

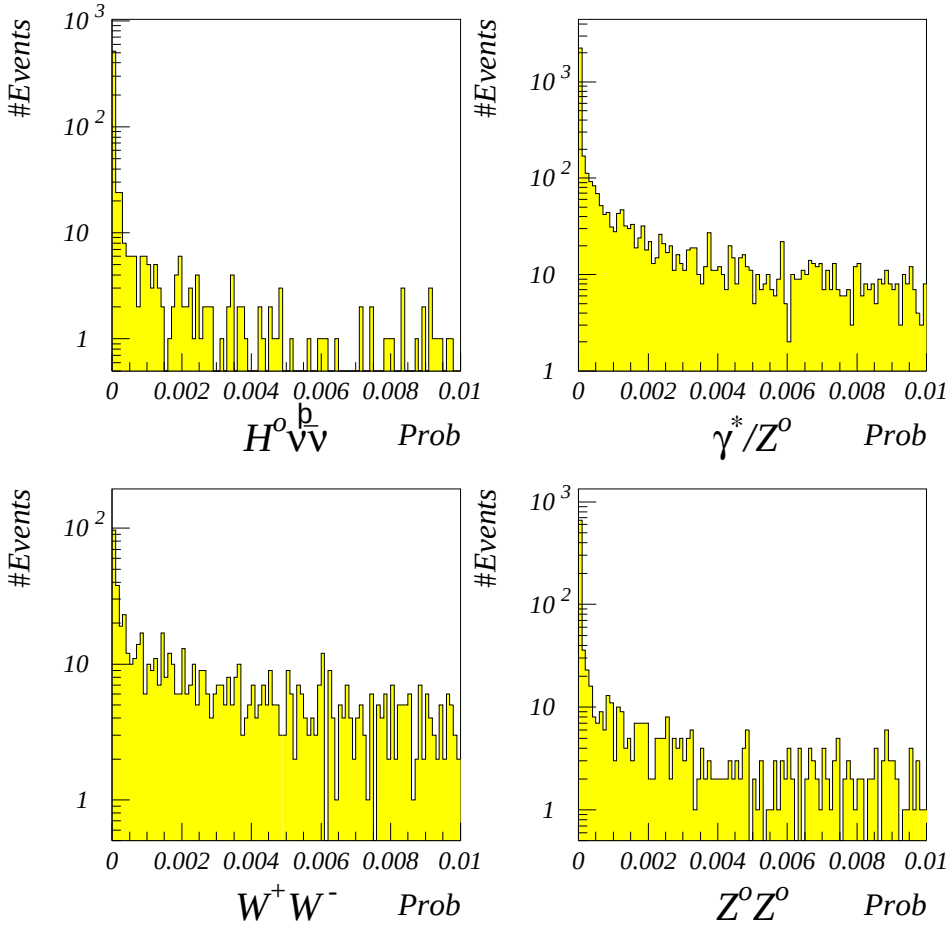

Figure 6.11: Positive N-track probabilities calculated using AABTAG. E_{cms} = 192 GeV and m_{H^0} = 90 GeV. Only probabilities ranging from 0 to 0.01 are shown.

6.10 Graphical cuts in acolinearity vs. total momentum

Two things have not been discussed yet. These are the magnitude of the total momentum and the acolinearity of the two jets. The acolinearity is defined as the complement of the angle between the two jets of the events. Recall that events with two jets have been selected. This means that if the angle between the two jets is θ, then the acolinearity will be $180 - \theta$. Separate cuts in these characteristics are possible, but it's immediately obvious that there is a strong correlation between them. An event with jets pointing in opposite directions, will have little acolinearity and the jet momenta will cancel each other leaving only a small magnitude of the total event momentum. On the other hand, jets pointing in the same direction will lead to a total momentum of great magnitude and naturally a large acolinearity. This strong correlation makes it worthwhile creating graphical event selections, or cuts, in total momentum versus acolinearity.

Different characteristics at different energies make it necessary to create dedicated scatter plots at each energy. Plots at 175, 192, and 205 GeV are presented in Fig. 6.12, Fig. 6.13 and Fig. 6.14 respectively. The graphical cut at 175 GeV was made using simulated data based on a Higgs mass of 80 GeV, the cut at 192 GeV used data based on a Higgs mass of 90 GeV, and finally the cut at 205 GeV used data based on $m_{H^0} = 100$ GeV.

The data displayed in the two-dimensional scatter plots had to undergo some very rudimentary initial cuts to make them suited for drawing of the graphical cuts. At 192 GeV, special data containing only $H^0\nu\bar{\nu}$ events were available, but this was not the case for the 175 GeV and 205 GeV simulated events. At these two energies, only H^0Z^0 events were available. These contain only 20% $H^0\nu\bar{\nu}$ events, leaving them unsuited for drawing of graphical cuts. Introducing a single restriction demanding exactly two jets, solved the problem and stripped away most of the unwanted events. This is naturally because most of the unwanted H^0Z^0 events contain four hadronic jets. After this simple cut, the H^0Z^0 data was ready for use in drawing of the graphical cuts. The two-dimensional plots show the very strong correlation between acolinearity and total momentum in the γ^*/Z^0 events. It's also clear that the $H^0\nu\bar{\nu}$ events tend to have quite small acolinearities and total momenta, separating them well from the background events. Properly chosen graphical cuts like those shown in the figures, reduce backgrounds a lot. The shape of the selected areas, or graphical cuts, is a bit peculiar, as ellipsoid shapes would have been anticipated. The reason is that few background events are located in the upper left corner of the selected areas of the scatter plots. This is particularly true when all other cuts have been applied. Expanding the selected areas to the upper left introduces considerable amounts of signal events, and almost no extra background. Separate cuts in acolinearity and total momentum also work, but give considerably worse results. The graphical

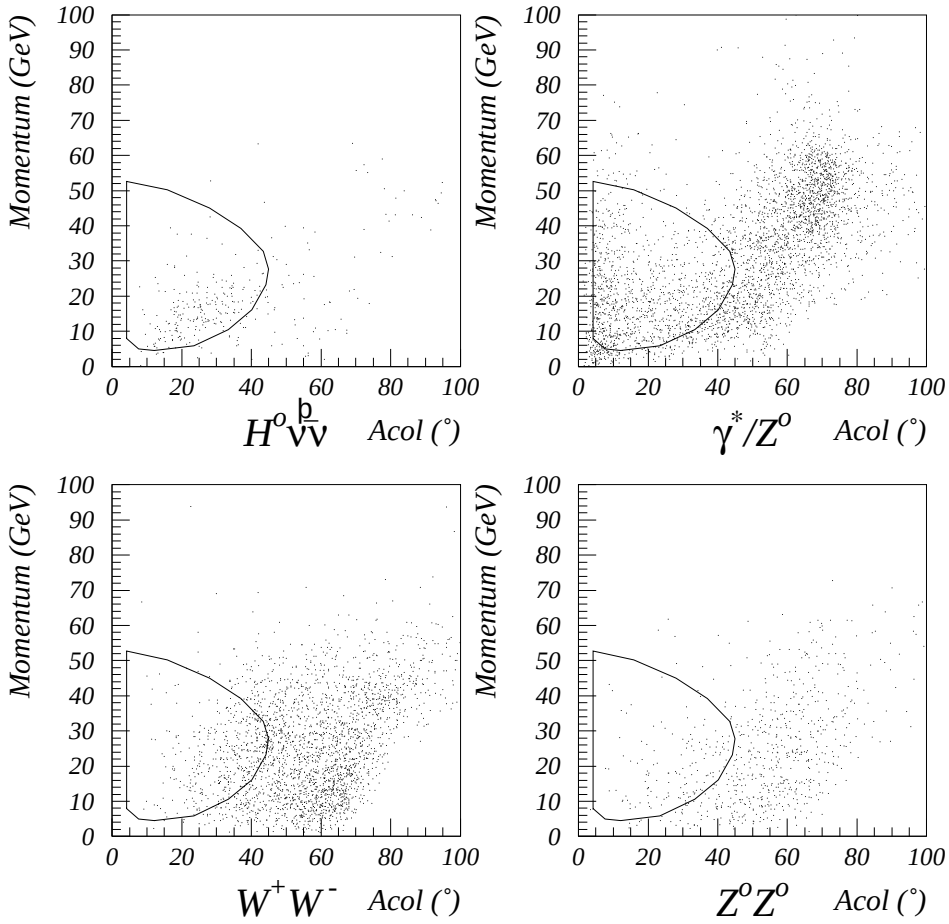

Figure 6.12: Graphical cut in acolinerarity vs. total momentum at 175 GeV, and $m_{H^0} = 80$ GeV.

cuts remove most of the remaining background events that survived all the other cuts.

The background events that survive look exactly like $H^0\nu\bar{\nu}$ events, they contain two B jets that point in opposite directions, have low total energy and large acoplanarities.

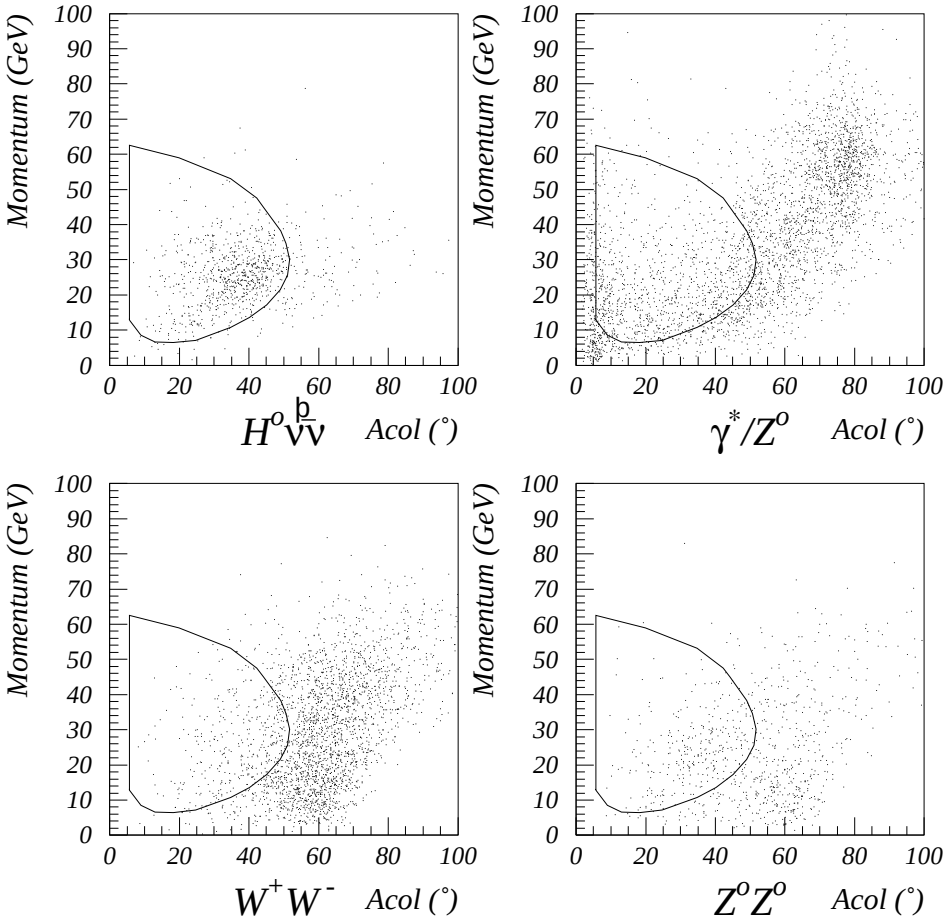

Figure 6.13: Graphical cut in acolinerarity vs. total momentum at 192 GeV, and $m_{H^0} = 90$ GeV.

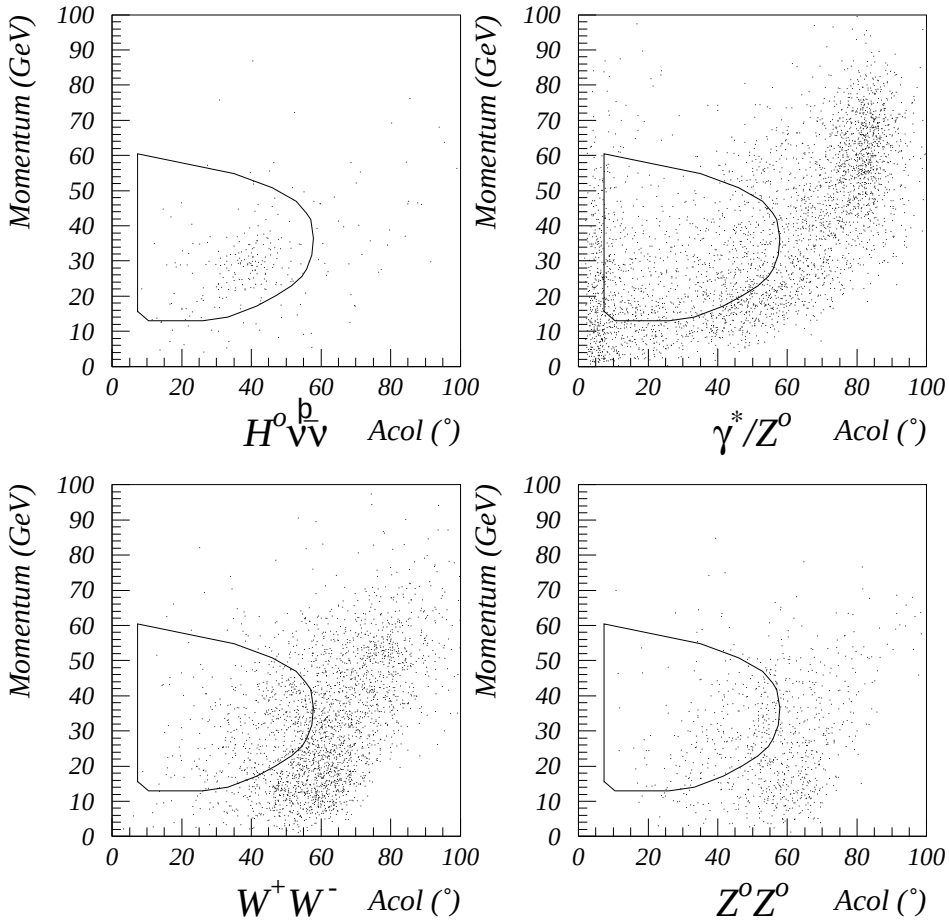

Figure 6.14: Graphical cut in acolinerarity vs. total momentum at 205 GeV, and $m_{H^0} = 100$ GeV.

6.11 Hits in the 40° taggers

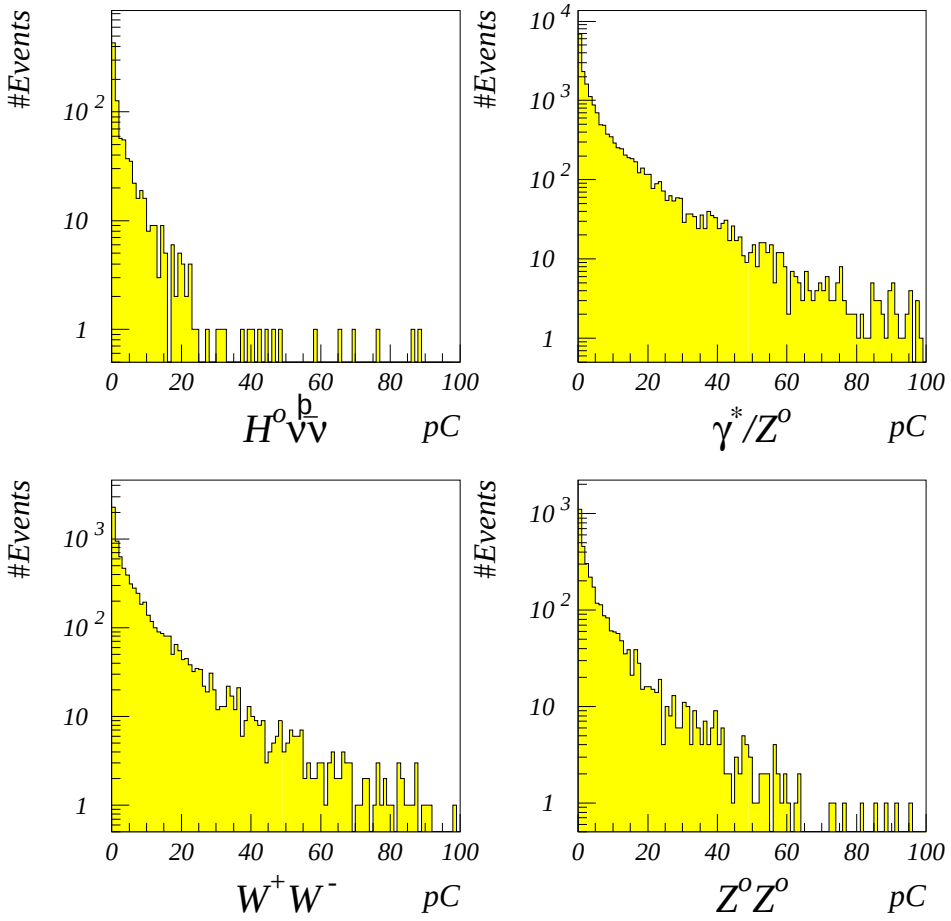

Figure 6.15: Total charge generated in the 40° taggers. E_{cms} = 192 GeV and m_{H^0} = 90 GeV.

It happens that the DELPHI detector lacks proper calorimetry in the 40° region. In other words, neutral particles emitted at 40° relative to the beam pipe often pass straight through the detector without detection. This is due to a very bad design of the barrel-endcap intersection. This unfortunate 40° crack is visible in Fig. 2.1 of chapter 2. To reduce this problem, it was recently decided to install some rather basic and crude detectors in these cracks. These 40° taggers are not suited for proper track reconstruction and they do not even give a good estimate of the momentum and energy of detected particles. As a result, detections in the 40° taggers are not included in the main banks of the data summary tapes,

but only in a small bank containing crude information directly from the taggers. Some of this information is displayed in Fig. 6.15, which shows the total charge, given in pico Colomb, generated in the 40° taggers, using a logarithmic scale.

At first glance the different distributions are very similar, and it seems like a very uninteresting characteristic to do a cut in. This is only until Table 6.3, has been studied. Surprisingly, the cut at 25 pC removes two out of the three remaining γ^*/Z^0 events! This is quite amazing and the cut removes some of the final events at 175 GeV and 205 GeV too. A closer study reveals that the two γ^*/Z^0 events removed at 192 GeV, have angles between the beam pipe and total momentum of, 46.4° and 48.1°. In other words, the missing momentum of these events points in the direction of the 40° cracks, clearly suggesting that the photons produced by radiative return to Z^0 has left the detector unnoticed through these cracks. Luckily these two escaping photons were detected by the 40° taggers, stopping the corresponding events from being accepted as Higgs events. The final γ^*/Z^0 event at 192 GeV has an angle of 74.8° between total momentum and beam pipe. The powerful γ of this event probably escaped through some crack other than the 40° crack, or possibly even through a defect detector module. As long as the DELPHI detector isn't hermetically closed, a few gammas will escape, opening the possibility of γ^*/Z^0 events being accepted as Higgs events.

6.12 Selections at all energies and their effect on data

This section is dedicated to various tables stating the selections applied at the three energies 175, 192, and 205 GeV, and showing the results of applying these cuts to the different backgrounds and the signal. The selections are tabulated in Table 6.1, while the effect of the selections on simulated data at 175, 192, and 205 GeV, are shown in Table 6.2, Table 6.3 and Table 6.4 respectively. The selections are applied cumulatively, one at a time.

Cuts applied at		*175 GeV*	*192 GeV*	*205 GeV*
Number of Jets	=	2	2	2
Rho	>	30°	27°	27°
Acoplanarity	>	9.0°	7.0°	7.0°
35.0 GeV < E_{vis}	<	85.0 GeV	95.0 GeV	105.0 GeV
Total STIC energy	<	1.0 GeV	1.0 GeV	1.0 GeV
Max FEMC hit	<	4.5 GeV	5.0 GeV	5.5 GeV
Max HPC hit	<	16.0 GeV	17.0 GeV	18.0 GeV
B tag	<	0.001	0.001	0.001
40° tag	<	24 pC	25 pC	26 pC
Plus Graphical cut in total momentum vs. acolinearity				

Table 6.1: The cuts applied at 175, 192, and 205 GeV.

Cuts at 175 GeV			H^0Z^0	$\gamma^\star/Z^0$	W^+W^-	Z^0Z^0
Initial events			999	27450	5017	1500
Number of Jets	=	2	304	14094	1863	559
Rho	>	30°	257	5755	1614	368
Acoplanarity	>	9.0°	137	843	1193	189
35.0 GeV < E_{vis}	<	85.0 GeV	112	466	554	97
Total STIC energy	<	1.0 GeV	94	200	478	83
Max FEMC hit	<	4.5 GeV	91	127	429	71
Max HPC hit	<	16.0 GeV	90	112	314	62
B tag	<	0.001	62	14	7	5
Graphical cut			50	2	0	3
40° tag	<	24 pC	47	1	0	3
Final events			47	1	0	3

Table 6.2: Number of events left after each cut at 175 GeV. $m_{H^0} = 80$ GeV was chosen for the H^0Z^0 signal. Cuts are applied cumulatively.

Cuts at 192 GeV			$H^0\nu\bar{\nu}$	$\gamma^\star/Z^0$	W^+W^-	Z^0Z^0
Initial events			1000	32377	8556	3958
Number of Jets	=	2	830	16205	3128	1401
Rho	>	27°	755	6963	2674	1146
Acoplanarity	>	7.0°	626	1370	2257	821
35.0 GeV < E_{vis}	<	95.0 GeV	597	829	1363	600
Total STIC energy	<	1.0 GeV	547	355	1158	537
Max FEMC hit	<	5.0 GeV	535	236	1027	511
Max HPC hit	<	17.0 GeV	511	203	698	471
B tag	<	0.001	360	21	20	99
Graphical cut			339	3	2	89
40° tag	<	25 pC	333	1	1	85
Final events			333	1	1	85

Table 6.3: Number of events left after each cut at 192 GeV. $m_{H^0} = 90$ GeV was chosen for the H^0Z^0 signal. Cuts are applied cumulatively.

Cuts at 205 GeV			H^0Z^0	$\gamma^\star/Z^0$	W^+W^-	Z^0Z^0
Initial events			999	36634	5003	998
Number of Jets	=	2	260	17798	1833	341
Rho	>	27°	221	7601	1525	266
Acoplanarity	>	7.0°	178	1589	1275	217
35.0 GeV < E_{vis}	<	105.0 GeV	145	1009	901	169
Total STIC energy	<	1.0 GeV	125	431	755	146
Max FEMC hit	<	5.5 GeV	119	289	665	137
Max HPC hit	<	18.0 GeV	115	231	446	119
B tag	<	0.001	81	22	18	23
Graphical cut			77	5	3	21
40° tag	<	26 pC	73	3	3	21
Final events			73	3	3	21

Table 6.4: Number of events left after each cut at 205 GeV. $m_{H^0} = 100$ GeV was chosen for the H^0Z^0 signal. Cuts are applied cumulatively.

Chapter 7

Final results

7.1 Signal efficiencies

All cuts and their effects on the different backgrounds have now been discussed, but a final summary of results has not been presented yet. This is the subject of this chapter.

Table 7.1, shows the efficiencies of the different Higgs signals that were simulated by DELSIM. The efficiencies are presented for different Higgs masses and energies. The signal events at $m_{H^0} = 90$, 95, and 100 GeV, and at $E_{cms} = 192$ GeV, are pure $H^0\nu\bar{\nu}$ events, but the rest of the signals are full H^0Z^0 simulations with only 20% $H^0\nu\bar{\nu}$ events. A separate column of expected signal events, at a total integrated luminosity of 500 pb^{-1}, at 175 GeV, and 300 pb^{-1}, at 192 and 205 GeV, has been included. It's immediately clear that only a few H^0Z^0 events, 9.7 at best, will be observed if the Higgs is light enough. The statistical errors of the signal efficiencies are given by the following formula

$$\sigma_\epsilon = \frac{\sqrt{\epsilon(1-\epsilon)}}{\sqrt{N}}$$

where N is the number of total signal events in each dataset, and ϵ is the corresponding signal efficiency. The statistical errors of both the signal efficiencies and the number of expected events have been included in Table 7.1. It is important to notice that even though the H^0Z^0 datasets contain 1000 events, only 200 of these are $H^0\nu\bar{\nu}$ events, which means that $N = 200$ when calculating uncertainties for these datasets. Strictly, this approach presumes that cuts designed to remove the background will also remove all background Higgs events, i.e. the Higgs events not belonging to the neutrino channel. This is not an unreasonable presumption to do, as the background Higgs events contain either $b\bar{b}q\bar{q}$ or $b\bar{b}l\bar{l}$ where l is a charged lepton. These events contain too many jets and have too high energy to be accepted as Higgs events of the neutrino channel. The cross sections of the various Higgs signals have also been included in the table, and the ones corresponding to the $H^0\nu\bar{\nu}$ signal have been adjusted to suit these events. These cross sections are only 20% of the full H^0Z^0 cross sections.

7.2 Total backgrounds and their statistical errors

Table 7.2 shows all background data available at $E_{cms} = 175$ GeV. In addition data at $E_{cms} = 170$ and 180 GeV have been added to increase statistics. These data were created, using DELSIM, right before it was decided to run simulations at 175, 192 and 205 GeV. This means that the version of DELSIM used at these simulations was very similar to the version used at the later 175, 192 and 205 GeV simulations. The difference in energy of the 170 and 180 GeV data relative

Signal	m_{H^0} (GeV)	*Accepted events*	*Efficiency* (%)	σ (pb)	*expected events*
175 GeV					500 pb^{-1}
H^0Z^0	80	47/999	24.5 ± 3.0	0.283	6.7 ± 0.8
H^0Z^0	85	45/999	23.5 ± 3.0	0.158	3.6 ± 0.5
192 GeV					300 pb^{-1}
H^0Z^0	80	30/1000	15.6 ± 2.6	0.594	5.4 ± 0.9
H^0Z^0	85	67/1000	34.9 ± 3.4	0.484	9.7 ± 0.9
$H^0\nu\bar{\nu}$	90	333/1000	33.3 ± 1.5	0.075	7.5 ± 0.3
$H^0\nu\bar{\nu}$	95	341/1000	34.1 ± 1.5	0.046	4.7 ± 0.2
$H^0\nu\bar{\nu}$	100	215/1000	21.5 ± 1.3	0.017	1.1 ± 0.1
205 GeV					300 pb^{-1}
H^0Z^0	90	56/999	29.2 ± 3.2	0.450	7.6 ± 0.8
H^0Z^0	100	71/999	37.0 ± 3.4	0.301	6.4 ± 0.6
H^0Z^0	105	78/999	40.7 ± 3.5	0.227	5.3 ± 0.5

Table 7.1: Signal efficiencies and their uncertainties.

to the desired 175 GeV data is unfortunate, but the huge increase of statistics is far more important than the slight variation of energy. This is particularly visible in Table 7.3, which presents all background data available at 192 GeV. If only the 192 GeV data were included the results for both the $\gamma^\star/Z^0$ and the W^+W^- backgrounds would be much better than the corresponding ones at 175 and 205 GeV. Instead, the great increase of statistics by the introduction of datasets of a slightly different *cms* energy, reduces the statistical errors by considerable amounts, thereby giving more reliable results. The $(e^+e^-)f\bar{f}$ events at 192 GeV were created using the DELPHI Monte Carlo program TWOGAM[17].

Background	E_{cms} (GeV)	*Accepted events*	σ (pb)	*expected events* 500 pb^{-1}
$\gamma^\star/Z^0$	170	1/30600	171	
	175	1/27450		
	180	1/22300		
		3/80350		3.2 ± 1.8
W^+W^-	175	0/5017	15.1	
	180	5/17340		
		5/22357		1.7 ± 0.8
Z^0Z^0	175	3/1500	0.46	0.5 ± 0.3
Weν	175	1/748	0.65	0.4 ± 0.4
Total events				5.8 ± 2.1

Table 7.2: Background events at $E_{cms} = 175$ GeV.

The statistical errors of the individual background processes are given by

$$\sigma_{bg} = k\sqrt{N_b(1 - \frac{N_b}{N_s})}$$

where k is a scaling factor given by N_{tot}/N_s. N_{tot} is the total number of events of a particular background at a given *cms* energy and integrated luminosity, and N_s is the total number of simulated events of the chosen background. N_b is the number of events passing the cuts. Individual statistical errors have been included in all three tables, as well as the total statistical error given by

$$\sigma_{tot} = \sqrt{\sigma^2_{\gamma^\star/Z^0} + \sigma^2_{W^+W^-} + \sigma^2_{Z^0Z^0} + \sigma^2_{We\nu}}$$

Background	E_{cms} (GeV)	*Accepted events*	σ (pb)	*expected events* 300 pb^{-1}
$\gamma^\star/\mathrm{Z}^0$	190	8/67000	136	
	192	1/32377		
		9/99377		3.7 ± 1.2
$\mathrm{W}^+\mathrm{W}^-$	190	6/10564	18.1	
	192	1/10243		
		7/20807		1.8 ± 0.7
$\mathrm{Z}^0\mathrm{Z}^0$	190	7/512	1.22	
	192	85/3958		
		92/4470		7.5 ± 0.8
$\mathrm{Z}^0\mathrm{e}^+\mathrm{e}^-$	190	0/1978	6.7	
	192	0/3220		
		0/5198		0
$(\mathrm{e}^+\mathrm{e}^-)f\bar{f}$	190	0/5896	25.0	
	192	0/2454		
		0/8350		0
Weν	190	1/997	0.83	0.2 ± 0.2
Total events				13.2 ± 1.6

Table 7.3: Background events at $E_{cms} = 192$ GeV.

Background	E_{cms} (GeV)	*Accepted events*	σ (pb)	*expected events* 300 pb^{-1}
$\gamma^\star/Z^0$	200	3/20300	115	
	205	3/36634		
	210	2/16000		
		8/72934		3.8 ± 1.3
W^+W^-	200	0/2110	18.3	
	205	3/5003		
	210	0/2397		
		3/9510		1.7 ± 1.0
Z^0Z^0	205	16/998	1.47	7.1 ± 1.8
$Z^0e^+e^-$	205	0/1491	7.3	0
Total events				12.6 ± 2.4

Table 7.4: Background events at $E_{cms} = 205$ GeV.

Errors of backgrounds with zero events passing the cuts are hard to fit into this scheme, but using Poisson statistics it's possible to estimate an upper limit of a particular background that seems to be totally removed. According to Poisson statistics, the expected background of $(e^+e^-)f\bar{f}$, at 192 GeV and integrated luminosity of 300 pb^{-1}, is less than 2.1 at 90% confidence level. The limit has been scaled to take both the number of $(e^+e^-)f\bar{f}$ events, at 192 GeV and 300 pb^{-1}, and the total number of simulated $(e^+e^-)f\bar{f}$ events into account. This upper limit of the $(e^+e^-)f\bar{f}$ background, is rather conservative though, as the $(e^+e^-)f\bar{f}$ events have a very strong bias in the forward direction. Circumstances have to be very special for a $(e^+e^-)f\bar{f}$ event to be mistaken as a $H^0\nu\bar{\nu}$ event. The cuts designed to remove the γ^*/Z^0 events, which also have a strong bias in the forward direction, are also very effective in removing the $(e^+e^-)f\bar{f}$ events. The few events that survive these cuts are removed by others, especially the strict B tag cut. The cross section of the presented $(e^+e^-)f\bar{f}$ events is far less than the cross section of the total $(e^+e^-)f\bar{f}$ background, because of severe introductory filtering of the data. This has been done to avoid a dataset completely crammed with empty events, as most of the fermions produced in this process pass out the beam pipe.

The other background to be treated by Poisson statistics is the $Z^0e^+e^-$ background, which is far more relevant as a dangerous background than the $(e^+e^-)f\bar{f}$ process. This background will eventually introduce Higgs-like events, though only a few at most. At 192 GeV and an integrated luminosity of 300 pb^{-1}, the upper limit at 90% confidence level is 0.9 using Poisson statistics. Again, the limit has been scaled to take both the number of background events, at 192 GeV and 300 pb^{-1}, and the number of simulated events into account. The reason for the much lower limit in this case compared to the previous $(e^+e^-)f\bar{f}$ limit, is the higher statistics relatively speaking. Unfortunately, the statistics of the $Z^0e^+e^-$ process are much lower at 205 GeV, with only 1491 simulated events compared to the 5198 simulated events at 192 GeV. This leads to an upper limit of 3.4 events for the $Z^0e^+e^-$ background, at 205 GeV, integrated luminosity of 300 pb^{-1}, and 90% confidence level, according to Poisson statistics. This upper limit is however very pessimistic, as the corresponding limit at 192 GeV is only 0.9 events at 90% confidence level.

One background, mentioned in chapter 4, has not been considered yet. This is the $Z^0\nu\bar{\nu}$ background. Unfortunately, no simulated events of this process were available to study, and available Monte Carlo programs did not have the process implemented. A closer look at the diagrams responsible for $Z^0\nu\bar{\nu}$ production reveals four bremsstrahlung diagrams with a Z^0 radiated off an electron or neutrino, one fusion diagram and two annihilation diagrams with a Z^0 radiated off a neutrino in the final state of the interaction. These diagrams are complicated and involve heavily suppressed couplings, leading to very low cross sections, at least at cms energies in the order of 200 GeV. In addition, the four bremsstrahlung diagrams involve a Z^0 radiated along the beam pipe, making the background very

vulnerable to the cuts imposed on the $\gamma^\star/Z^0$ background. These considerations lead to a probable cross section, of the $Z^0\nu\bar{\nu}$ background, of the order of a few picobarn at most.

Looking at the tables presenting the expected events of the analysed backgrounds, the Z^0Z^0 process alone turns out to be responsible for more than half of the total background at 192 and 205 GeV. This has been discussed in previous chapters, and the reason is, as mentioned, the fraction of Z^0Z^0 events that decay into $b\bar{b}\nu\bar{\nu}$. The center of mass energy of simulations at 175 GeV is right below the threshold of Z^0Z^0 production, and the few Z^0Z^0 events produced are all crippled by one or two off-shell Z^0 bosons. These off-shell Z^0 bosons exhibited bad behavior in replicating Higgs bosons, as they usually decay into jets of few particles and low energy.

7.3 Exclusion and Discovery limits

E_{cms} (GeV)	$\int L\mathrm{d}t$ (pb^{-1})	*Background*	*Exclusion* (signal events)	*Discovery* (signal events)
175	500	5.8 ± 2.1	7.3	17.4
192	300	13.2 ± 1.6	9.2	22.5
205	300	12.6 ± 2.4	9.3	22.5

Table 7.5: Number of signal events needed for exclusion and discovery, at the three energies.

Exclusion and discovery limits, calculated with the prescription agreed on by all LEP experiments[18], are presented in Table 7.5. The exclusion limits are at 95% confidence level using Poisson statistics, and the discovery limits are at approximately $5\sqrt{bg}$, where bg is the number of background events. Calculation of the limits is based on expected integrated luminosity, number of background events and their uncertainties.

7.4 Conclusion

Comparing Table 7.5 with Table 7.1, it immediately becomes clear that the expected number of signal events at various energies and Higgs masses is far too low for any discovery, and only in two cases, at $E_{cms} = 192$ GeV and $m_{H^0} = 85$ or 90 GeV, is the number of signal events above the exclusion limit. It is however important to remember that the neutrino channel treated in this thesis is only 20% of the total H^0Z^0 signal. The quark and lepton channels of the H^0Z^0 signal

have been studied in great detail too, and adding results of all three channels improves the results a lot. Adding all channels, it is possible for DELPHI to exclude a Higgs boson of up to 96 GeV mass, at $E_{cms} = 192$ GeV and integrated luminosity of 300 pb^{-1}, while discovery is possible for a Higgs boson of up to 90 GeV mass.

These results are good and covers a wide range of Higgs masses not accessible at the old LEP accelerator, and probably not at the future Large Hadron Collider, either. Higgs masses of less than 100 GeV are very hard to study at the LHC, because of modest Higgs production and severe background. Combining results of all four LEP experiments will give even better results and allow discovery of a Higgs boson of up to 96 GeV mass, and exclusion of a Higgs boson of 99 GeV mass or less, at $E_{cms} = 192$ GeV and integrated luminosity of 300 pb^{-1} for each experiment. If not found at LEP200, the search for the Higgs boson will continue with full strength at LHC. At LHC other modes of Higgs production will be studied and circumstances will be very different from the ones at LEP200. The background will be severe, entirely dwarfing the LEP200 background, but the Higgs production will also be much bigger than the one at LEP200, if the Higgs boson really exists. The only thing certain is that Higgs searches at LEP200 and LHC will keep particle physicists and students busy for many years to come.

Bibliography

[1] A. Sopczak, *Status of Higgs Hunting at LEP - Five Years of Progress*, HEP-PH-9504300, PPE Division, CERN.

[2] DELPHI Collaboration, *Nuclear Instruments and Methods in Physics Research* **A303** (1991) 233-276.

[3] F. Stichelbaut, *Study of the Performance of the 40° Counters with the 94 Data*, CERN, PPE division.

[4] J.F. Gunion, H.E. Haber, G. Kane and S. Dawson, *The Higgs Hunters Guide.* Frontiers in Physics Series (Vol.80), ISBN 0-201-50935-0. 1990.

[5] P. W. Higgs, *Phys. Lett.* **12** (1964) 132, *Phys. Rev. Lett.* **13** (1964) 508, *Phys. Rev.* **145** (1966) 1156; F.Englert and R. Brout, *Phys. Rev. Lett* **13** (1964) 321; G.S. Guralnik, C.R Hagen and T.W.B. Kibble, *Phys. Rev. Lett* **13** (1964) 585; T.W.B. Kibble, *Phys. Rev.* **155** (1967) 1554.

[6] J.S. Bell, *Nucl. Phys.* **B60** (1973) 427; C.H. Llewellyn Smith, *Phys. Lett.* **46B** (1973) 233; J.M. Cornwall, D.N. Levin, and G. Tiktopoulos, *Phys. Rev. Lett.* **30** (1973) 1268, and *Phys. Rev.* **D10** (1974) 1145.

[7] J. Björken, *Proceedings of the 1976 SLAC summer Institute on Particle Physics*, ed. by M.C. Zipf (SLAC Report 198, 1977) p. 1.

[8] Bernd A. Kniehl, Institut für Theoretische Physik, Universität Hamburg. Eilam Gross, Gustavo Wolf, Weizmann Institute of Science, Israel. *Production and Decay of the Standard Model Higgs Boson at LEP200*, DESY 94-035.

[9] H.-U. Bengtsson and T. Sjöstrand, Computer Physics Commun. **46** (1987) 43.

[10] T.Sjöstrand, Computer Physics Commun. **39** (1986) 347; T.Sjöstrand and M. Bengtsson, Computer Physics Commun. **43** (1987) 367.

[11] DELPHI Collaboration, DELPHI 89-67 PROG 142, 10 Jul 1989.

[12] T.Sjöstrand, Computer Physics Commun. LUCLUS is part of the Pythia Monte Carlo program.

[13] D. Brown and M. Frank, *Tagging b hadrons using track impact parameter*, ALEPH 92-135, PHYSIC 92-124.

[14] DELPHI collaboration, DELPHI 89-44 PROG 137, 17 May 1989.

[15] DELPHI Collaboration, DELPHI 94-161 PROG 210, 20 Dec 1994.

[16] G.V. Borisov, *Lifetime Tag of events $Z^0 \to b\bar{b}$ with the DELPHI detector. AABTAG program.* DELPHI 94-125 PROG 208, 11 August 1994.

[17] S. Nova et al. *MONTE-CARLO Event Generator for two Photon Physics.* DELPHI 90-35 PROG 152, 19 November 1990.

[18] Appendix, *Interim report on the physics motivations for an energy upgrade of LEP*, by the Workshop on Physics at LEP200, CERN-TH/95-151, CERN-PPE/95-78.